ENGINYERIA ELECTRÒNICA ELÈCTRICA I AUTOMÀTICA

UNIVERSITAT ROVIRA I VIRGILI

Graduate Students Meeting on Electronics Engineering

Tarragona, Spain. June 30 - July 01, 2016

BOOK OF ABSTRACTS

DIPUTACIÓ DE TARRAGONA

IEEE

FUNDACIÓ URV

ENGINYERIA ELECTRÒNICA ELÈCTRICA I AUTOMÀTICA

UNIVERSITAT ROVIRA I VIRGILI

Graduate Students Meeting on Electronics Engineering

Tarragona, Spain. June 30 - July 01, 2016

Programme

ENGINYERIA ELECTRÒNICA ELÈCTRICA I AUTOMÀTICA

UNIVERSITAT ROVIRA I VIRGILI

Graduate Students Meeting on Electronics Engineering

Tarragona, June 30th and July 1st of 2016

Programme

Thursday, June 30th

14:50 15:00 Check-In and Poster Placement
15.00 Opening
15.05 - 16.00 Invited talk: "Scopes of devices and techniques pioneered by the Engineers used in the health system: wearable ECG monitoring, fetal ECG and walking age".
Dr. Tapas Mondal. Department of Pediatrics. Mac Master University, Canada.

16:00 - 17:00 Students Presentations:

16.00: Fabrication of Back-Gated Device for Gas Sensors. Tesfalem Geremariam Welearegay (Minos)

16.20: 1H-NMR-based metabolomics: Different "ways" to analyse complex data. Rubén Barrilero (SiPOmicS)

16.40: Frequency Selective Surface backscatter modulated tag and reader prototype for wearable sensor applications. Javier Lorenzo (NePhoS)

17:00 Afternoon Break and Poster Session

Friday, July 1ST

09:00 - 10:00 Invited Talk: "Enabling technologies for future healthcare based on breath analysis".
Dr. Sergi Udina JLM Innovation GmbH, Alemanya.

10:00 – 10:40 Students Presentations:

10.00: From raw data to biological insights: data processing in mass spectrometry-based metabolomics. Xavi Domingo (SiPOmicS)

10.20: Modeling Approach for Rapid NEGF-Based Simulation of Ballistic Current in Ultra-Short DG MOSFETs. Fabian Hosenfeld (NePhoS)

10:40 – 11:00 Coffee break

11:00 - 12:00 Invited Talk: "Engineering Education and Economic Development - Fact or Fiction"
Dr. Jamal Deen. Department of Electrical and Computer Engineering. Mac Master University, Canada.

12:00 -13:00 Students Presentations:

12:00: Synthesis of Single Crystalline In2O3 octahedra for detecting oxidizing and reducing gases at trace levels. Sergio Roso (Minos)

12:20: Fabrication, Characterization and Stability Analysis of Inverted Polymer Solar Cells. José Guadalupe Sánchez (NePhoS)

12:40: Fluid Imbibition-Coupled Laser Interferometry: a highly sensitive optical technique for nanometrology. Chris Eckstein (NePhoS)

13:00 Clossing Session and Lunch

ENGINYERIA ELECTRÒNICA ELÈCTRICA I AUTOMÀTICA

UNIVERSITAT ROVIRA I VIRGILI

Graduate Students Meeting on Electronics Engineering

Tarragona, Spain. June 30 - July 01, 2016

Invited Sessions

ENGINYERIA ELECTRÒNICA ELÈCTRICA I AUTOMÀTICA
UNIVERSITAT ROVIRA I VIRGILI
Graduate Students Meeting on Electronics Engineering
Tarragona, June 30th and July 1st of 2016

Enabling technologies for future healthcare based on breath analysis.

Dr. Sergi Udina

R&D Director
JLM Innovation GmbH

Abstract
At present, strong efforts are being placed in the transfer of breakthrough laboratory results regarding medical diagnosis through breath analysis, into point-of-care technologies. The immense technological challenges that his technology transfer process has to face can be easily underestimated when considering some of the still preliminary, but very promising results already published.
A look into the specific scientific and technological challenges involved reveals the necessity of strong synergies between fields so apparently disparate as sensor development and production, high-performance electronics, novel microfluidics, multivariate data analysis, smartphones and even Big data.
The talk is aimed as a walkthrough across the current status of the breath analysis field, current developments, and the many strong challenges that wait on the road to a practical implementation of widespread breath analysis techniques in the healthcare scenario, including point-of-care technologies, and smartphone assisted healthcare (or mobile health). Hopefully we will be able to get a glimpse into the future of the field.

ENGINYERIA ELECTRÒNICA ELÈCTRICA I AUTOMÀTICA

UNIVERSITAT ROVIRA I VIRGILI

Graduate Students Meeting on Electronics Engineering

Tarragona, Spain. June 30 - July 01, 2016

Regular Sessions

Analytical Modeling of Intrinsic Capacitance of Double-Gate Tunnel-FETs

Atieh Farokhnejad[1, 2,*], Michael Graef[1, 2], Fabian Hosenfeld[1, 2], Fabian Horst[1, 2], Benjamín Iñíguez[2], François Lime[2], Alexander Kloes[1]
[1]Competence Centre for Nanotechnology and Photonics, Technische Hochschule Mittelhessen, Giessen, Germany
[2]DEEEA, University Rovira i Virgili, Tarragona, Spain
*atieh.farokhnejad@ei.thm.de

Abstract

Considering the Tunnel-FET has become one of the most promising candidate to be the surrogate of the standard MOSFET technology, device characterization is gaining more importance. This paper presents an AC-model for a Double-Gate (DG) Tunnel-FET. By means of the carrier concentration, the intrinsic capacitances in a Si DG n-Tunnel-FET are calculated. To verify the model, the results are compared with TCAD Sentaurus simulations. The model represents a particularly good manifestation of the device AC behavior and is a good estimation.

1. Introduction

When it comes to the nanoscale electronics and technology, the Tunnel-FETs are in the center of the attractions. This ever increasing interest owes to their feasibility to overcome the 60 mV/dec subthreshold slope limitation of the standard MOSFETs [1]. In order to get a solid grasp of the Tunnel-FETs working principle and showing their behavior in all operating regions, different models should be taken into account.

In this paper the AC-model, also known as small-signal model, is considered. This model is used for frequency analysis and describes mainly the capacitive behavior of the transistor [2].

The goal of this work is indeed, analytical modeling of the intrinsic capacitances in a DG Tunnel-FET. The device which is modeled, is a Si DG n-Tunnel-FET with a high p-doped source region N_s=10^{20} cm^{-3}, a high n-doped drain region N_d=10^{20} cm^{-3} and an intrinsic channel (see Fig. 1). The dimensions of the device are selected as following: l_{sd} = 20 nm, t = 10 nm, w_{ch} = 1 µm and t_{ox} = 2 nm. Moreover the high k oxide material HfO2 is used in the structure.

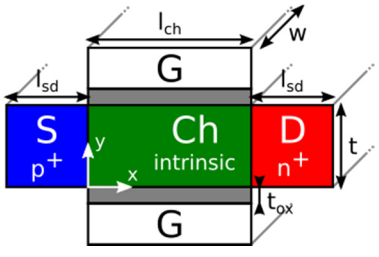

Fig. 1. Device geometry of a DG n-Tunnel-FET, showing its structural parameters and doping.

For the verification of the model, the obtained results are compared with the TCAD simulation data. Furthermore, to inspect the scalability of the model, various l_{ch} and V_d are examined.

2. Capacitance Modeling

The charges which are stored in the transistor give cause for capacitive behavior of the device [2]. In Figure 2 some of the capacitances in a DG Tunnel-FET are shown. Here, the focus is on intrinsic capacitances which are distinct in the figure.

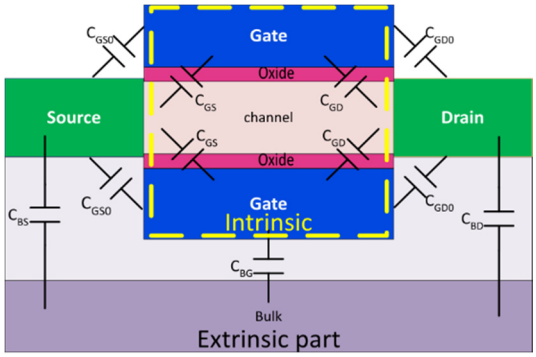

Fig. 2. Capacitances in a DG Tunnel-FET, whereby the modeling approach focuses on the intrinsic capacitances.

To calculate the C_{gd} and C_{gs}, firstly the charge density in the region between gate, drain and source must be calculated.

It is assumed that the charges are uniformly distributed in the whole channel. The reason is, that in Tunnel-FET, in contrast with MOSFET, the barrier is the bottleneck for the current flow and the voltage drop happens mainly in the barrier rather all along the channel. According to this assumptions and considering the inversion charge at the potential barrier in a multi-gate device [3], the charge density at the drain end is given as following

$$Q'_d = 2C'_{eff}V_{th}\alpha \times \mathcal{L}\left(\frac{Q'_{io}\cdot\exp\left(\frac{2C'_{eff}(V_g - V_d - V_0) + Q'_{io}}{2C'_{eff}V_{th}\alpha}\right)}{2C'_{eff}V_{th}\alpha}\right). \quad (1)$$

Where V_{th} is the thermal voltage, α is the slope degradation factor which expresses the ratio between the degraded and the ideal slope and Q'_{io} is the integral inversion charge for an arbitrary gate bias of V_0 in the

subthreshold regime [3]. The $\mathcal{L}$ in this formula is the first branch of Lambert's W function [4]. The C'_{eff} represents the effective capacitance including oxide and depletion capacitances in series and is given by

$$C'_{eff} = \frac{1}{1/C'_{ox} + 1/C'_{dep}}. \quad (2)$$

The C'_{ox} and C'_{dep} are achieved from $\frac{\varepsilon_{ox}}{t_{ox}}$ and $\frac{\varepsilon_{si}}{t_{dep}}$, where ε_{ox} and ε_{Si} refer to the gate oxide and Si permittivity. Here, t_{dep} is a fitting parameter, which indicates the distance between the charge centroid and the oxide interface.

In the same way, just by applying the source voltage, the Q'_s is obtained.

If it is assumed the potential barrier is located in a distance of x_b from source junction, the total inversion channel charge associated with drain and source are obtained from

$$Q_{ch,d} = Q'_d W_{ch}(l_{ch} - x_b) \quad (3)$$

and

$$Q_{ch,s} = Q'_s W_{ch}(l_{ch} - x_b). \quad (4)$$

The parameters are channel width W_{ch}, channel length l_{ch} and the effective channel length $(l_{ch} - x_b)$. Now, it is possible to calculate C_{gd} and C_{gs} considering the changes in total charge in accordance with changes in V_g as following

$$C_{gd} = \frac{\Delta Q_{ch,d}}{\Delta V_g} \quad (5)$$

and then as well

$$C_{gs} = \frac{\Delta Q_{ch,s}}{\Delta V_g}. \quad (6)$$

3. Results

In this section the results obtained from analytical model are compared with the TCAD simulations data. Figure 3 illustrates the C_{gd} as a function of the gate voltage and drain voltage. The channel length in this case is equal to 30 nm.

Increasing the V_d leads to a shift of the Fermi potential and it lowers the charge attribution to the drain. This is the reason why in Figure 3 by increasing the V_d the C_{gd} decreases.

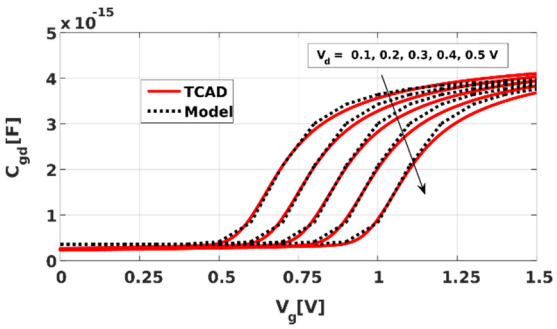

Fig. 3. C_{gd} for various drain voltages.
α= 1.58, x_b= 3 nm, t_{dep}= 0.53 nm and l_{ch} = 30 nm.

Figure 4 depicts the comparison between the modeled gate-source capacitance and TCAD simulation data, considering different l_{ch}. In Figure 5 one can see the gate-gate capacitance of the DG-n-Tunnel-FET, which is in principle the summation of C_{gd} and C_{gs}, as a function of V_g and different l_{ch}.

The longer the channel is the more charges exist in the channel, and thus a bigger capacitance is expected. In Figure 4 and 5 it can be seen, that the model almost fulfills the expectation as good as the TCAD simulations.

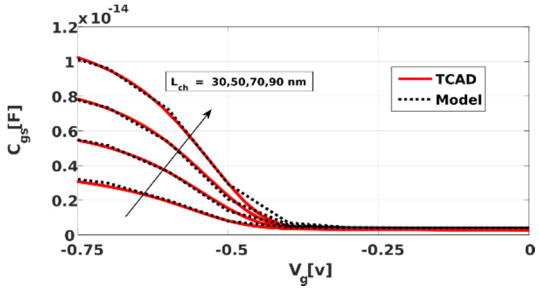

Fig. 4. C_{gs} for various channel lengths.
α= 1.50 to 1.58, x_b= 3 nm, t_{dep}= 0.53 nm and V_d = 0.2 V.

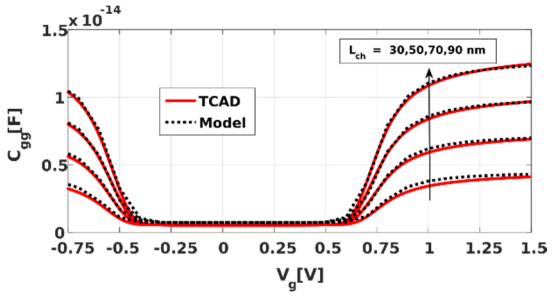

Fig. 5. C_{gg} for various channel lengths.
α= 1.50 to 1.58, x_b= 3 nm, t_{dep}= 0.53 nm and V_d = 0.2 V.

4. Conclusions

In this paper an analytical model of the intrinsic capacitances in a DG Tunnel-FET is presented. Although it is tried to avoid complexities in this model and is kept as simple as possible, the model represents a good manifestation of the device AC behavior. The modeling results are in a good agreement with the TCAD simulations.

5. Acknowledgement

This project is supported by the German Federal Ministry of Education and Research under contract No. FKZ03FH010IX5. We would like to thank Keysight Technologies for the license donation of the software IC-CAP and AdMOS GmbH for support.

References

[1] H. Lu and A. Seabaugh, "Tunnel Field-Effect Transistors: State-of-the-Art," *Electron Devices Society, IEEE Journal, vol. 2, pp. 44-49*, 2014.

[2] N. Arora, Mosfet modeling for VLSI simulation: theory and practice, World Scientific , 2007.

[3] A. Kloes, M. Schwarz, T. Holtij and A. Navas, "Quantum Confinement and Volume Inversion in MOS3 Model for Short-Channel Tri-Gate MOSFETs," *Electron Devices, IEEE Transactions, vol. 60, pp. 2691–2694*, Aug 2013.

[4] R. M. Corless, G. H. Gonnet, D. E. G. Hare, D. J. Jef and D. E. Knuth, "On the Lambert W Function," *Adv. Comput. Math., vol. 5, pp. 329–359*, Feb. 1996.

SLIDING-MODE CONTROL OF A BOOST CONVERTER SUPPLYING A CONSTANT POWER LOAD.

Blanca A. Martinez -Treviño, Robin Jammes, Abdelali El Aroudi, Luis Martinez -Salamero.

Departament d'Enginyeria Electrònica, Elèctrica i Automàtica, Universitat Rovira i Virgili (URV), Campus Sescelades, Avinguda Països Catalans 26, 43007 Tarragona, Spain, e-mail: luis.martinez@urv.cat

Abstract

Cascade connection of DC-DC switching converters is often required in multi-converter systems with the aim of distributing power in electric vehicles, renewable energy installations, electric aircrafts and space systems. In the connection of two converters, the first one is called source while the second one is denominated load. The operation of the load converter absorbing constant power can provoke unstable behavior in the cascade connection, the optimal solution of this problem being still open.

The work here reported tackles the problem of controlling in sliding-mode a boost converter supplying a constant power load (CPL). A combination of two switching surfaces is employed, so that the first one is used for starting-up while the second one regulates the output voltage in steady-state. A detailed analysis showing the converter trajectories in the phase–plane and the conditions for the existence of sliding-mode are presented. The analytical predictions are in perfect agreement with PSIM and MATLAB simulations.

1. Boost converter with CPL

Figure 1 shows a boost converter supplying a constant power load (CPL), which is characterized by the current –voltage relationship $i_{CPL} = \frac{P}{v_c}$, where P is the power absorbed by the load.

The corresponding state equations can be expressed in compact form as follows:

$$\frac{dv_C}{dt} = \frac{i_L}{C}(1-u) - \frac{P}{Cv_C}$$

$$\frac{di_L}{dt} = -\frac{v_C}{L}(1-u) + \frac{V_g}{L} \qquad (1)$$

Where *u=1* during T_{ON} and *u=0* during T_{OFF}

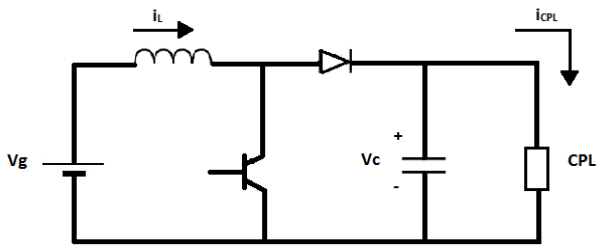

Figure 1. Boost converter with CPL

Solving the differential equations for *u=1* and *u=0* leads to the phase-plane trajectories during *on* and *off* states given below

For *u=1*

$$i_L = \frac{CVg}{2PL}(v_C(0)^2 - v_C{}^2) + i_L{}^2 \qquad (2)$$

For *u=0*

$$i_L(t) = -\frac{1}{L}\int_0^t v_C(\lambda)d\lambda + \frac{Vg}{L}t + i_L(T_{OFF}) \qquad (3)$$

$$\frac{d^2v_c}{dt^2} - \frac{P}{C}\frac{1}{v_c^2}\frac{dv_c}{dt} + \frac{v_c}{CL} = \frac{V_g}{LC} \qquad (4)$$

Note that both trajectories denote a clear unstable behavior.

On the other hand, the equilibrium points locus (EPL) is obtained assuming that the derivatives of the trajectories in the phase plane are opposite with equal absolute value

$$\left.\frac{dv_C}{di_L}\right|_{T_{ON}} = \left.\frac{dv_C}{di_L}\right|_{T_{OFF}} \qquad (5)$$

From (5) we derive

$$\frac{-\frac{P}{Cv_C}}{\frac{Vg}{L}} = \frac{\frac{1}{C}\left(i_L - \frac{P}{v_C}\right)}{\frac{1}{L}(Vg - v_C)} \qquad (6)$$

Solving (6) results in

$$i_L = \frac{P}{V_g} \qquad (7)$$

2. Switching surface and control law

In order to drive the system to EPL in spite of the unstable behavior of on and off states, the following nonlinear surface is proposed:

$$s_1(x) = v_C i_L - V_{CREF} \cdot I_{LREF} + K_1(v_c - V_{CREF}) \qquad (8)$$

The corresponding control law is given by

$$\begin{aligned} u &= 0 \quad s > 0 \\ u &= 0 \quad s > 0 \end{aligned} \qquad (9)$$

Also, for sliding-mode existence the following conditions must be satisfied:

$$\left.\begin{aligned} \dot{s}_1(x) < 0 \ \ when \ \ s_1 > 0 \\ \dot{s}_1(x) > 0 \ \ when \ \ s_1 < 0 \end{aligned}\right\} s_1 \dot{s}_1(x) < 0 \qquad (10)$$

From (8), it can be derived

$$\dot{s}_1(x) = \frac{d}{dt}(v_C i_L - V_{CREF} \cdot I_{LREF} + K_1(v_c - V_{CREF}) \qquad (11)$$

Hence

$$\dot{s}_1(x) = i_L \frac{dv_c}{dt} + v_c \frac{di_L}{dt} + K_1 \frac{dv_c}{dt} \qquad (12)$$

Taking into account (1) and (12), it is obtained

$$\frac{{i_L}^2}{C} - \frac{{v_c}^2}{L} + \frac{K_1 i_L}{C} < 0 \qquad (13)$$

Equivalently,

$$v_c > \sqrt{\frac{L}{C}\left({i_L}^2 + K_1 i_L\right)} \qquad (14)$$

Figure 2 illustrates the regions for existence of sliding – mode, the straight line representing EPL and the switching surface.

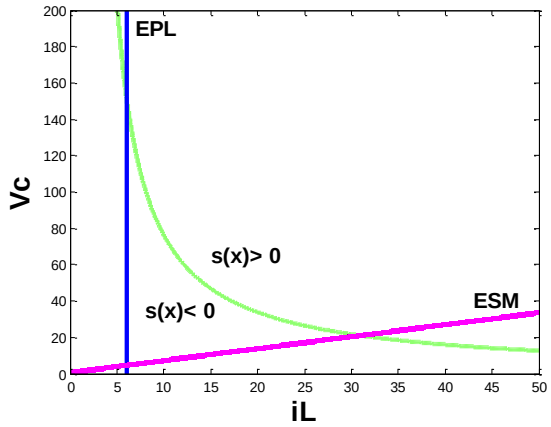

Figure 2. Switching surface, EPL and regions for existence of ESM

Besides, the ideal sliding dynamics corresponding to the average trajectory of the converter on the switching surface will be expressed in terms of the equivalent control (u_{eq}) by imposing the conditions $s_1(x)=0$

$$\frac{ds_1}{dt} = 0 \Longrightarrow u = u_{eq} \qquad (15)$$

Hence,

$$\left(\frac{(i_L + K_1)i_L}{C} - \frac{{v_c}^2}{L}\right)(1 - u_{eq}) - \frac{(i_L + K_1)P}{Cv_c} = 0 \qquad (16)$$

Solving for (16)

$$u_{eq} = \frac{L(i_L + K_1)(v_c i_L - P) - C{v_c}^2(V_g - v_c)}{v_c[L(i_L + K_1)i_L - C{v_c}^2]} \qquad (17)$$

In steady- state:

$$u_{eq_{ss}} = \frac{V_{CREF} - V_g}{V_{CREF}} \qquad (18)$$

Note that (18) is bounded between 0 and 1, as it could be expected-

It can be observed that the coordinates of the equilibrium point are given by

$$I_{LREF} = \frac{P}{V_g} = {i_L}^* \qquad (19)$$

$$V_{CREF} = v_c^* \qquad (20)$$

The proposed sliding mode control is validated by the PSIM simulation shown in Figure. 3 , which corresponds to the set of parameters

$$P = 200\ W$$
$$Vg = 33\ V$$
$$V_{CREF} = 150\ V$$
$$I_{LREF} = P/Vg$$
$$L = 0.0433\ mH$$
$$C = 100\mu F$$
$$K1 = 2$$
$$I(0) = 2\ A$$
$$V(0) = 1\ V$$

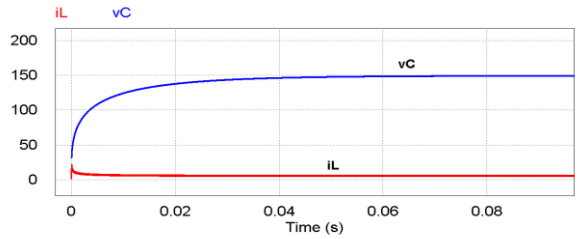

Figure 3.Output voltage and current waveforms

The corresponding behavior in the phase-plane is described in the MATLAB simulation depicted in Figure 4.

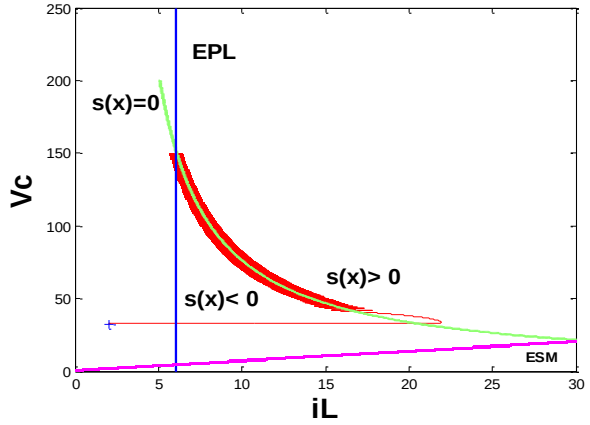

Figure 4. Output voltage/current of the boost converter and the equilibrium points shown in MATLAB

3. Switching surface modification

In order to avoid the high value of the load current during start-up and the associated large inrush current, a linear switching surface is proposed for starting-up together with an auxiliary diode connecting input and output voltages. The expression of the new switching surface is given by

$$s_2(x) = K_c(V_{CREF} - v_c) + K_i(I_{LREF} - i_L) \quad (21)$$

Once that the converter trajectory is approaching the first surface $s_1(x)$ the control system will deactivated $s_2(x)$ and the regulation will be carried out by $s_1(x)$.

Figures. 5 and 6 show the correct operation of the control based on the mentioned two surfaces. The change of surface takes place when the capacitor voltage reaches *100V.*

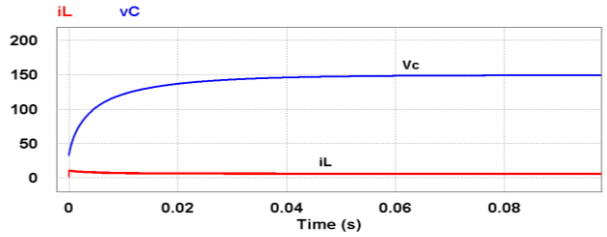

Figure 5. Current and voltage waveforms when s1 and s2 are combined

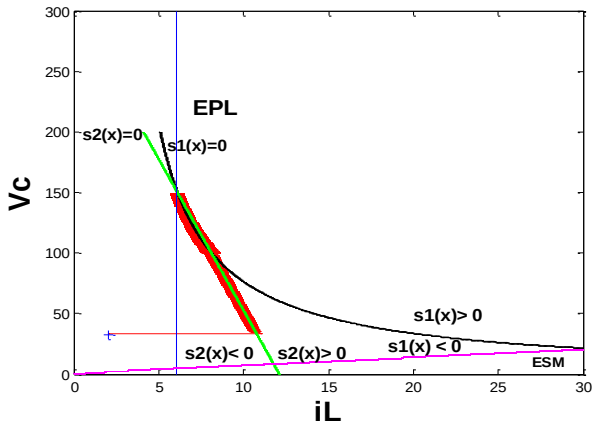

Figure 6 Phase-Plane trajectory when s1 and s2 are combined

4. Conclusions

Sliding-mode control based on the use of two switching surfaces has been proved to be an effective solution to regulate a boost converter feeding a constant power load. The theoretical predictions have been verified by PSIM and MATLAB simulations. Further research contemplates the implementation of a prototype for experimental verification.

References

[1] Amir M. Rahimi and Ali Emadi, "Active Damping in DC/DC Power Electronic Converter: A novel Method to overcome the Problems of Constant Power Loads. *IEEE Trans. Ind. Electron., vol.56, no.5,May.2009*

[2] V.I Utkin, J.Gulder, and J.Shi "Sliding –Mode Control in Electromechanical Systems" 2nd edition. Boca Ratón, Fl, *CRC Press*, 2009.

Optofluidic Biosensing via Capillary Filling in Nanoporous Anodic Alumina

Chris Eckstein, Elisabet Xifré-Pérez, Maria Porta-i-Batalla Josep Ferré-Borrull, Lluis F. Marsal

Departament d'Enginyeria Electrònica, Elèctrica i Automàtica, Universitat, Rovira i Virgili, Avda. Països Catalans 26, Tarragona 43007, Spain. Contact via chris.eckstein@urv.cat or +34601625951

Abstract

Fluid imbibition-coupled laser interferometry is an optofluidic technique which monitors light interferences of a laser beam caused by capillary filling in real-time. Processing the interference data, results in an estimate of the pore radius. Here we address the accuracy of this technique to detect small pore radius changes due to wet chemical etching and protein immobilization. We found that FICLI provides more accurate estimations of pore radius changes than traditional ESEM image analysis. Furthermore, the immobilization of proteins inside the pores was detected and estimates of the pore radius changes are in good agreement with previously reported protein sizes. FICLI is demonstrated as an accurate technique for the characterization of nanochannels across different liquid-surface interfaces and for biosensing applications.

Introduction

Nanoporous anodic alumina (NAA) has been previously demonstrated as a feasible carrier matrix for optofluidic characterization and sensing devices. NAA shows great tissue compatibility und is easily modified by wet chemical pore widening and conjugation of biomolecules to the inside walls of the pores [1–3].
Fluid imbibition-coupled laser interferometry (FICLI) has previously been presented as a novel optofluidic technique to estimate the pore radius of NAA by monitoring capillary filling time [4].

In this study we monitor light intensity fluctuations of a single wavelength in real-time and consider the time differences between two adjacent extrema as the basis to estimate the pore radius. We experimentally determine the accuracy of FICLI to detect changes in pore radius in the nanometer range upon wet chemical pore widening steps. We also address the applicability of this technique across different liquid-surface interfaces by using different liquids. Further, the repeatability and accuracy of radius reductions due to protein immobilization in NAA pores of varying as-produced pore radii is addressed. Finally, the capability of sensing a multi-step immobilization of Protein A and antibody binding is studied.

Materials & Methods

Sample fabrication (in brief)

NAA of 75µm thickness were produced in oxalic acid electrolyte following a two-step anodization protocol. The aluminum bottom was removed by a mixture of $CuCl_2$-HCl (saturated) and 68% HNO_3 and the pores were opened by reactive ion etching. The pore radius was increased by stepwise wet chemical etching with a controlled pore widening time t_{PW}. The pore walls were subsequently hydroxylated in > 30% H_2O_2 and incubated with protein solutions at 4°C overnight.

FICLI

The light intensity of a laser beam reflected off the bottom of an NAA is registered over time. Capillary forces readily draw in a liquid dropped onto the NAA.

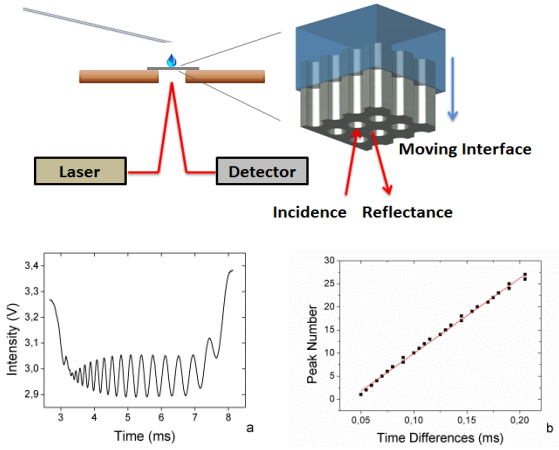

Figure 1: experimental set-up, raw data and time differences over indexed extrema pair.

The moving liquid interface within the pores changes the optical path between the two reflected waves leading to successive intensity extrema. The extrema in the pattern are indexed and the time of occurrence is registered. The time difference between two consecutive extrema is plotted against the extremum index, producing a linear trend. The pore radius can then be estimated from the slope of this linear trend (S) with the expression:

$$R_0 = \left(\frac{\alpha {L_0}^6}{S}\right)^{\frac{1}{5}} \text{ with } \alpha = \frac{4\mu}{\pi^2 \gamma \cos\theta} \text{ and } {L_0}^3 = \frac{\lambda}{4(n_2 - n_3)\delta}.$$

Results and Discussion

Figure 2 shows the estimated pore radius (r) as a function of pore widening time (t_{PW}) obtained by FICLI using DI water, ethanol and 2-propanol. The pore radii estimated by ESEM image analysis are further presented. Similar pore etching rates of 0.85nm/min. for the three different liquids were found with a marginal deviation of 2nm between the liquids. The standard errors obtained by the ESEM image analysis resulted in a much larger error range. These findings demonstrate the applicability across different surface-matrix interfaces. The large standard error in the ESEM images makes FICLI more accurate towards the detection of minor changes in pore radius.

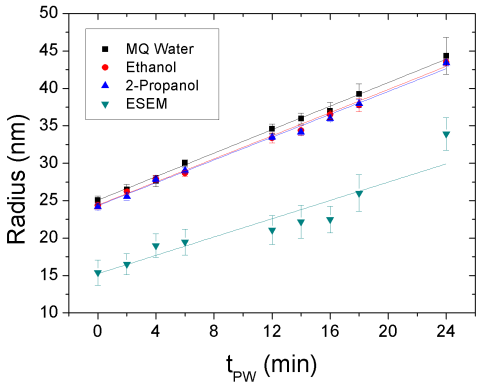

Figure 2: Estimated pore radii as a function pore widening time t_{PW}, obtained by FICLI using different liquids and ESEM image analysis.

Figure 3 shows the estimated pore radii of three samples with pores widened for the duration of t_{PW}. The immobilization of BSA within the three respective NAA is further illustrated. The pore radius reductions for the three NAA upon BSA immobilization are constant (d_{BSA} = 5.8nm) and fall in the size range expected for this protein according to its previously reported dimensions.

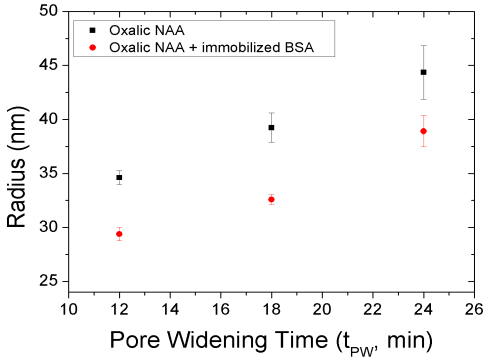

Figure 3: Pore radii estimated by FICLI as a function of pore widening time t_{PW} obtained before and after the immobilization of BSA.

Figure 4 shows the estimated pore radius of an NAA before and after two protein immobilization steps. The electrostatically immobilized Protein A reduced the pore radius by 4.6 nm, which represents the size of this protein according to the literature. The further reduction of the radius by 7.0 nm due to the binding of an antibody via its Fc portion to the Protein A also falls into the size range of an antibody.

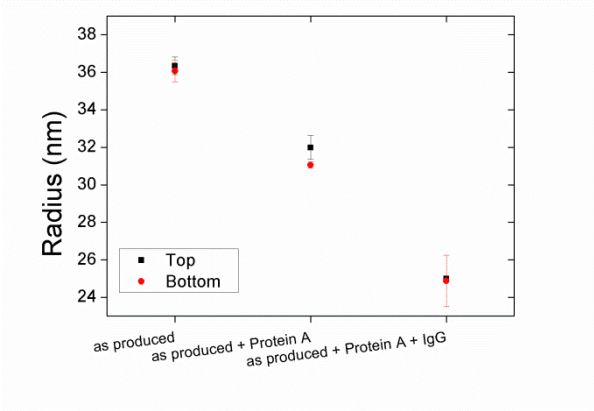

Figure 4: Pore radii estimated by FICLI before and after the immobilization of Protein A and antibody binding.

Conclusion

We demonstrated the applicability of FICLI as an accurate nanochannel characterization technique by showing similar pore etching rates for various liquids in accordance to the literature, with a resolution of 0.4nm maximal standard deviation. We successfully demonstrated the biosensing accuracy and repeatability via the immobilization of BSA and the subsequent pore radius reduction of 5.8nm within nanochannels of different pore radii. The estimated size of BSA is in good agreement with the literature. The detection of the stepwise immobilization of Protein A and binding of antibody show good applicability of the method across different liquid-surface interfaces and the specific detection of targeted biomolecules.

References

(1) Macias, G.; Ferré-Borrull, J.; Pallarès, J.; Marsal, L. F. Effect of Pore Diameter in Nanoporous Anodic Alumina Optical Biosensors. Analyst 2014.

(2) Baranowska, M.; Slota, A. J.; Eravuchira, P. J.; Macias, G.; Xifré-Pérez, E.; Pallares, J.; Ferré-Borrull, J.; Marsal, L. F. Protein Attachment to Nanoporous Anodic Alumina for Biotechnological Applications: Influence of Pore Size, Protein Size and Functionalization Path. *Colloids Surf. B. Biointerfaces* **2014**, *122*, 375–383.

(3) Dhathathreyan, A. Real-Time Monitoring of Invertase Activity Immobilized in Nanoporous Aluminum Oxide. *J. Phys. Chem. B* **2011**, *115* (20), 6678–6682.

(4) Urteaga, R.; Acquaroli, L. N.; Koropecki, R. R.; Santos, A.; Alba, M.; Pallarès, J.; Marsal, L. F.; Berli, C. L. A.; Marsal, F.; Berli, C. L. A. Optofluidic Characterization of Nanoporous Membranes. *Langmuir* **2013**, *29* (8), 2784–2789.

Synthesis of new organic semiconductor molecules as HTM in Perovskites Solar Cells: main features.

Cristina R. Seco[a], Lydia Cabau[*,a] and Emilio Palomares[a,b].

[a]*Institute of Chemical Research of Catalonia (ICIQ), Avinguda del Països Catalans 16, 43007 Tarragona, Spain. Fax: +34 977 920 823; Tel: +34 977 920 200; E-mail: lcabau@iciq.es*
[b]*Catalan Institution for Research and Advanced Studies (ICREA), Passeig de Lluis Companys 23, 08010 Barcelona, Spain.*

Abstract

The lead halide perovskite solar cells (PSCs) have attracted many interest because of its easy and low cost fabrication process, besides that the fact of its high efficiency. However, the most efficient and used organic hole transporting material (HTM) is too expensive and not easy to sensitize: 2,2′7,7′-tetrakis-(N,N-di-p-methoxyphenyl-amine)-9,9′-spirobifluorene (spiro-MeOTAD). The aim of this thesis thesis is not only design and synthesize new HTM if not the study of the energy losses due to the HTM and try to modify them for a better performance in Perovskite Solar cells. Here, the most important properties of a good HTM are shown and some examples of new small molecules as HTM applying all of these principles.

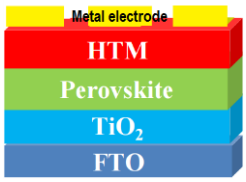

Figure 1: Schematic diagram of perovskite solar cell (PSC).

1. Introduction

Since the seminal paper of Miyasaka and co-workers [1] lead halide Perovskite (PSC) has become the focus of intense research due to its outstanding performance in hybrid photovoltaic devices. HTM in PSC play a key role increasing the efficiency producing an efficient hole transport and carry them to the metal electrode. The most used HTM Is the 2,2′7,7′-tetrakis-(N,N-di-p-methoxyphenyl-amine)-9,9′-spirobifluorene (spiro-MeOTAD). However the hight cost associated to it, and the multi-step synthesis required doesn't make this HTM suitable for practical applications. Polymers widely used in Organic Solar cells (OPV) have been tested as HTM for PSC With promising results as for example poly(3-hexylthiophene) P3HT or poly-triarylamine PTAA [4, 5] . Many Small molecules have been synthesized and tested achieving high Photovoltaic conversion efficiencies [6]. These last HTM present more practical applications than polymers due to its easy tunable properties or the easy design, synthesis and reproducibility. The work in this thesis is the study of different HTM designed and synthesized in the lab and tested in PSCs not only with the aim of achieves higher efficiency than Spiro-OMeTAD if not to understand the process that occur in the complete devices (Charge injection and Recombination process…).

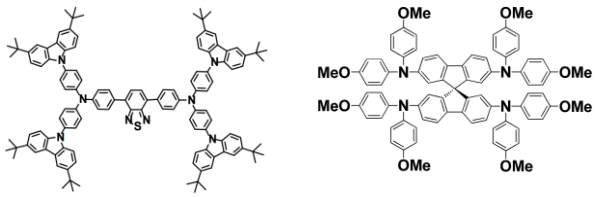

Figure 2: Molecular structures of spiro-MeOTAD and BCPA-B. [2]

One of the approaches of the synthesis of these new HTM arises from the fact the use of different additives needed for Spiro OMeTAD decreasing the stability of the devices. We want to synthesize new HTM that present an easy synthesis and long thermal stability without the needed to use extra additives.

2. New HTM

Many HTMs have been synthetized with different donor moieties and structures by the use of triphenylamine (TPA)-based, carbazole derivatives and

other derivatives in star-shape structures planar or spiro among others obtaining good photovoltaic performances in most of the different structures.

Four new HTM have been designed and synthesized (Scheme 1 and 2) to be tested and deeply study in complete devices. The different molecules have different parts in common in order to be feasible their study using homemade systems to study the charge kinetics as for example the Photo-Induce Charge Extraction (PICE), Photo-Induce Transient Photovoltage (PITPV), Photo-Induce Transient photocurrent (PITPC), Differential Charging (DC) or Laser Transient Absorption Spectroscopy (L-TAS) among others.

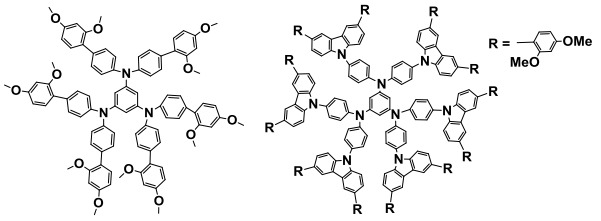

Scheme 1: CS05 and CS06.

As we said above some parts of the different molecules are the same. CS05 and CS06 show the same core (benzene) and also the same R-group attached to TPA and Carbazole respectively. Also we can observe that the structure of CS05, CS06 and CS07 is based in a star that can help to have a better interaction between the HTM the perovskite surface. On the other hand The introduction of another TPA group can change the HOMO (Highest Occupied Molecular Orbital) and LUMO (Lowest Unoccupied Molecular Orbital) changing the V_{oc} explaining better the origin of this Voltage in these devices.

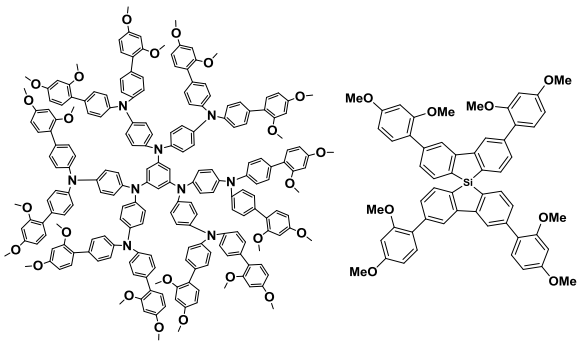

Scheme 2: CS07 and CS08.

3. Results and conclusion

The most important conclusion is that the HTM plays an important role in the Perovskite Solar cells to achieve good photovoltaic performance and achieve a right charge separation transport and collection in the electrodes. Knowing that HTM can be directly related with the increase in the V_{oc} is important to study the different recombination process associated to V_{oc} losses and trying to reduce them. So it is needed to understand all these parameters and to study all processes that occur in PSC to continue improving new HTMs. Some HTMs are designed to synthesize during this year to achieve the aim of the project.

Before using these molecules in PSC, it is needed their physical characterization and calculate their energy levels that must be fit with perovskite's. With this HTM we expected to achieve a similar efficiency as the obtained with spiro-OMeTAD, achieve more stability without the use of additives or, at least, understand better how HTM work in PSC.

4. References

[1] | N. J. Jeon, H. G. Lee, Y. C. Kim, J. Seo, J. H. Noh, J. Lee, and S. Il Seok, "o-Methoxy Substituents in Spiro-OMeTAD for Efficient Inorganic− Organic Hybrid Perovskite Solar Cells", J. Am. Chem. Soc. 2014, 136, 7837−7840.

[2] T. Khanasa, "Bis(carbazol-9-ylphenyl)aniline End-Capped Oligoarylenes as Solution-Processed Nondoped Emitters for Full-Emission Color Tuning Organic Light-Emitting Diodes ", J. Org. Chem. 2013, 78, 6702−6713.

[3] T. Krishanamoorthy, F. Kunwu, P. P. Boix, H. Li, T. M. Koh, W. L. Leong, S. Powar, A. Grimsdale, M. Grätzel, N. Mathews, S. G. Mhaisalkar, J. Mater. Chem. A 2014, 2, 6305.

[4] N. J. Jeon, J. H. Noh, M. K. Nazeeruddin, M. Grätzel, S. I. Seok, J. Am. Chem. Soc. 2013, 135, 19087.

[5] H. Li, K. Fu, P. P. Boix, L. H. Wong, A. Hagfeldt, M. Gräztel, S. G. Mhaisalkar, A. C. Grimsdale, ChemSuSChem 2014, 7, 3420.

[6] J. Liu, Y. Wu, C. Qin, X. Yang, T. Yasuda, A. Islam, K. Zhang, W. Peng, W. Chen, L. Han, Energy Environ. Sci. 2014, 7
2963.

Implementation of a DC Compact Model for Double-Gate Tunnel-FET Based on 2D Calculations

F. Horst[1,2,✠], M. Graef[1,2], F. Hosenfeld[1,2], A. Farokhnejad[1,2] , B. Iñíguez[2] and A. Kloes[1]
[1]Competence Centre for Nanotechnology and Photonics, Technische Hochschule Mittelhessen, Giessen, Germany
[2]DEEEA, Universitat Rovira i Virgili, Tarragona, Spain
✠fabian.horst@ei.thm.de

***Abstract*—This paper introduces a two-dimensional physics-based compact model for a double-gate (DG) Tunnel-FET (TFET) implemented in Verilog-A. The compact model is derived from an analytical model published in [1], [2], [3]. Measurement data are used to verify and show the flexibility of the modeling approach. The simulation results of the compact model are good in agreement with the measurements. Advantages and limitations of the compact model are analyzed and discussed.**

***Keywords*—Compact modeling, Verilog-A, Double-Gate (DG) Tunnel-FET, Nanowire GAA Tunnel-FET.**

I. Introduction

Tunnel-field-effect transistors (TFETs), based on the band-to-band (B2B) tunneling mechanism, are the most promising devices to be the successor of the common MOSFET technology. As a result of the B2B tunneling mechanism, the subthreshold slope (S) is no longer limited to 60 $\frac{mV}{dec}$ in contrast to the MOSFET technology [4]. To simulate circuit applications and their behavior, the request for a compact model is omnipresent. Some models for DG TFETs implemented in Verilog-A have already been published. In [5] only the on-state current is modeled, whereas the ambipolar current has been neglected. Therefore the model is only useful for ideal TFET devices. But in real TFET devices the ambipolar-state is always an issue which has to be taken into account for performance estimation on circuits. So, this work introduces a two-dimensional physics-based compact model of a DG TFET, implemented in Verilog-A, which contains both, the ambipolar and on-state.

II. Modeling Approach

In this section the 2D physics-based compact modeling derivation for the on-state of a DG TFET is presented, which is transferred to the ambipolar state at the end of this section. The schematic device geometry is shown in Figure 1. The main

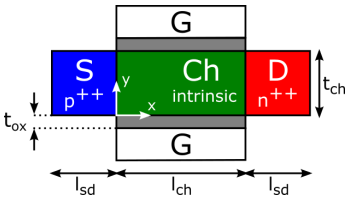

Figure 1. Schematic device geometry of a n-type DG TFET.

goal of this compact model is the description of an analytical model presented in [1], [2], [3]. Therefor, mathematical functions must be found, which are integrable in a closed form to qualify the resulting tunneling current of the device.

Thus, in the first step of the model derivation the electrostatic potential of the device must be approximated in the source and channel region. The potential within the source region for an arbitrary y-position can be described by a parabolic function (~x^2) and the channel potential is approximated with a rational function (~$1/x$), whereby the needed points of the approximation are calculated using the closed-form potential solution obtained in [3]. Applying the potential solution within the source and channel region the band structure in these regions can be approximated in order to qualify a function for the tunneling distance l_{tun}.

In the second step, the tunneling generation rate TGR along the x-axis for an arbitrary y-position must be qualified. A schematic sketch of the TGR is shown in Figure 2 (a). Applying two values of the analytical solution of the TGR (see eqn (35) in [1]) the compact TGR can be approximated with the help of the Gaussian distribution. The first point is calculated in the maximum of the analytical TGR, applying the first derivation of l_{tun} to get the value for x_{max}. The maximum of the TGR occurs at the position where l_{tun} has its minimum. The second point is calculated at the position $x_2 = x_{max} + \Delta x$, whereby $x_2 \leq l_{ch}$. Now, the compact TGR can be calculated and integrated for an arbitrary y-position along the x-axis. The integration of the TGR leads to the current density J_y along the y-axis (see blue dots in Figure 2 (b)), that is given by

$$J_y(y) = \frac{\mu_{tun,n} \cdot N_v \cdot q^2}{k \cdot T} \cdot \int_{x_{tun}}^{l_{ch}} TGR_n(x,y)\, dx, \quad (1)$$

with the channel length l_{ch}, and x_{tun} is the position where the conduction band in channel region overlaps the valence band in source region, so that B2B tunneling is possible

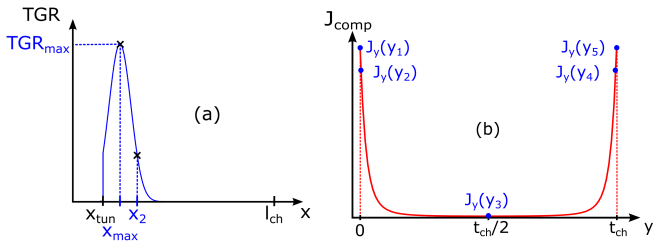

Figure 2. (a) Schematic shape of the $TGR(x,y)$ along the x-axis for an arbitrary y-position. (b) Schematic shape of the compact current density $J_{comp}(y)$ along the y-axis, which is approximated applying five points $J_y(y_1) \ldots J_y(y_5)$. $J_y(y_i)$ is the integration of the TGR along the x-axis.

The next step is the approximation of the compact current density $J_{comp}(y)$ along the y-axis as it is shown in Figure 2 (b). Therefore, J_{comp} is separated into two intervals, the first one is defined from 0 to $t_{ch}/2$ and the second one

from $t_{ch}/2$ to t_{ch}, whereby t_{ch} is the channel thickness. Both intervals are assumed to be shaped like Gaussian distribution with its maximum at $J_y(y_1)$ and $J_y(y_5)$, respectively. Hence, the compact current density for the first interval $J_{comp,\mathrm{I}}$ and the second interval $J_{comp,\mathrm{II}}$ can be calculated in the following way:

$$J_{comp,\mathrm{I/II}}(y) = \Big(J_y(y_{1/5}) - J_y(y_3)\Big) \times \exp\left(-\frac{(y-y_{1/5})^2}{\sigma^2_{\mathrm{I/II}}}\right) + J_y(y_3), \quad (2)$$

with $\sigma^2_{\mathrm{I/II}} = -(y_{2/4} - y_{1/5})^2 / \ln(J_y(y_{2/4})/J_y(y_{1/5}))$ and $J_y(y_3)$ compensates the offset in the channel center.

The compact tunneling current $I_{comp,on}$ for the on-state can be solved in a closed-form by integrating equation (2) separately for both intervals, which leads to

$$I_{comp,on} = \int_0^{\frac{t_{ch}}{2}} J_{comp,\mathrm{I}}(y)\, dy + \int_{\frac{t_{ch}}{2}}^{t_{ch}} J_{comp,\mathrm{II}}(y)\, dy. \quad (3)$$

The calculation of the compact tunneling current of the ambipolar-state $I_{comp,amb}$ is done in the same way as $I_{comp,on}$ considering the drain-to-channel junction and the physical parameters of the hole carriers. Hence, the compact tunneling current results in summation of both parts.

III. Model Verification

In this section, the compact model is compared to measurements of complementary strained Silicon nanowire (NW) GAA TFETs with 60 parallel NWs per device [6], applying the device geometry parameters of one NW: $l_{ch} = 350\,\mathrm{nm}$, $t_{ch} = 5\,\mathrm{nm}$, $t_{ox} = 3\,\mathrm{nm}$ and $w_{ch} = 40\,\mathrm{nm}$. Due to the channel width of one NW $w_{ch} >> t_{ch}$, the contribution of the gate at the front and backside of the NW can be adapted with the model fitting. Thus, we are able to apply the compact model of the DG TFET to this device structure. Figure 3 presents the current transfer characteristic of the n-type GAA TFET compared to the compact model. The model matches well

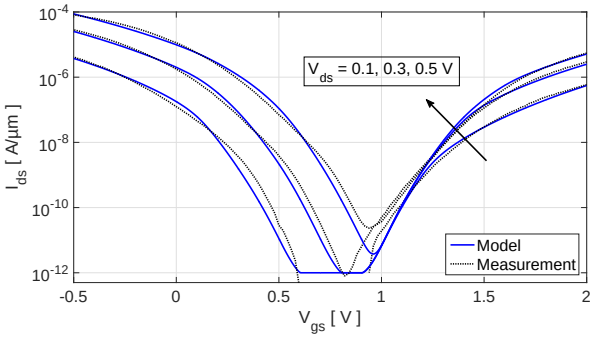

Figure 3. Transfer curve of the n-type GAA TFET compared to the compact model. Following parameters are applied: $\mu_{tun,n,(p)} = 5, (20)\,\mathrm{cm}^2/\mathrm{Vs}$, $m_{n,(p)} = 0.38, (0.38) \cdot m_0$ and $N_{s,(d)} = 3, (3) \cdot 10^{20}\,\mathrm{cm}^{-3}$.

with the measurement data with one exception at the transition from the ambipolar to the on-state. The reason for this is the missing trap-assisted tunneling (TAT) current, which has a major impact on the resulting subthreshold slope. In [2] a TAT model is presented which is implemented in the analytical model but not yet in the compact model.

The p-type model is emulated from the n-type model and Figure 4 illustrates the transfer curve of the p-type compact model in contrast to the measured data of the p-type GAA TFET [6]. The modeling results fit well with the measurement data. The only deviation occurs at the transition from the on- to the ambipolar-state because of the missing TAT model.

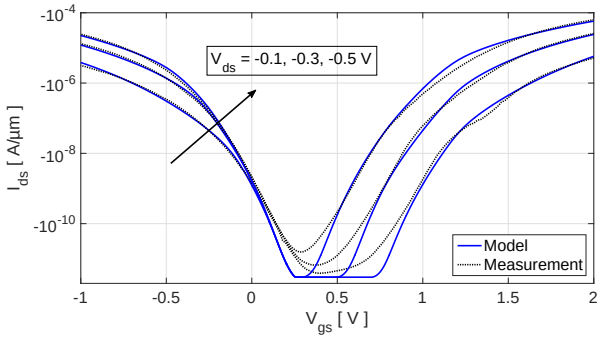

Figure 4. Transfer curve of the p-type GAA TFET compared to the compact model. Following parameters are applied: $\mu_{tun,n,(p)} = 2, (13)\,\mathrm{cm}^2/\mathrm{Vs}$, $m_{n,(p)} = 0.35, (0.35) \cdot m_0$ and $N_{s,(d)} = 2.5, (3) \cdot 10^{20}\,\mathrm{cm}^{-3}$.

IV. Conclusion

This paper introduced an innovative 2D physics-based compact model for DG TFETs implemented in the hardware description language Verilog-A. The model adapts a given analytical model with the help of mathematical functions to describe the electrical DC behavior of the DG TFET. The compact model has been verified by measurements and matches well with given data.

Acknowledgment

This project was supported by the German Federal Ministry of Education and Research under contract No. FKZ 03FH010IX5. We would like to thank Keysight Technologies for the license donation and support of the software IC-CAP and AdMOS GmbH for support. Furthermore, we would like to thank the PGI-9 IT from the Forschungszentrum Jülich for providing the measurement data.

References

[1] M. Graef, T. Holtij, F. Hain, A. Kloes, and B. Iñíguez, "A 2D Closed Form Model for the Electrostatics in Hetero-Junction Double-Gate Tunnel-FETs for Calculation of Band-to-Band Tunneling Current," *Microelectronics Journal*, vol. 45, no. 9, pp. 1144–1153, 2014.

[2] M. Graef, T. Holtij, F. Hain, A. Kloes, and B. Iñíguez, "Two-Dimensional Modeling of an Ultra-Thin Body Single-Gate Si Tunnel-FET," in *Ultimate Integration on Silicon (ULIS)*, pp. 101–104, IEEE, 2014.

[3] M. Graef, T. Holtij, F. Hain, A. Kloes, and B. Iniguez, "Improved Analytical Potential Modeling in Double-Gate Tunnel-FETs," in *Mixed Design of Integrated Circuits & Systems (MIXDES), 2014 Proceedings of the 21st International Conference*, pp. 49–53, IEEE, 2014.

[4] A. C. Seabaugh and Q. Zhang, "Low-Voltage Tunnel Transistors for Beyond CMOS Logic," *Proceedings of the IEEE*, vol. 98, no. 12, pp. 2095–2110, 2010.

[5] L. Zhang, J. He, and M. Chan, "A Compact Model for Double-Gate Tunneling Field-Effect-Transistors and Its Implications on circuit behaviors." Electron Devices Meeting (IEDM), 2012 IEEE International.

[6] G. Luong, S. Strangio, A. Tiedemannn, S. Lenk, S. Trellenkamp, K. Bourdelle, Q. Zhao, and S. Mantl, "Experimental demonstration of strained Si nanowire GAA n-TFETs and inverter operation with complementary TFET logic at low supply voltages," *Solid-State Electronics*, vol. 115, pp. 152–159, 2016.

Modeling Approach for Rapid NEGF-Based Simulation of Ballistic Current in Ultra-Short DG MOSFETs

F. Hosenfeld[1,2,✠], M. Graef[1,2], F. Horst[1,2], A. Farokhnejad[1,2], F. Lime[2], B. Iñíguez[2], A. Kloes[1]
[1]Competence Centre for Nanotechnology and Photonics, Technische Hochschule Mittelhessen, Giessen, Germany
[2]DEEEA, Universitat Rovira i Virgili, Tarragona, Spain
✠Fabian.Hosenfeld@ei.thm.de

***Abstract*—Multiscale simulation has to bridge the gap between device simulation, its effects in the atomic scale and the calculation of the device terminal voltages for circuit simulation. Iterative numerical solutions in device models significantly slow down the simulation. In this work a semi analytical non-equilibrium Green's function (NEGF) model for ultra-short DG MOSFETs is introduced, which turns the NEGF from an iterative numerical solution into a straightforward calculation. The benefit of using the NEGF is the physics-based consideration of quantum effects like the source-to-drain (SD) tunneling, which influences the device behavior in the sub 10 nm region. Using mathematical approximations, the calculation time of the 1D NEGF is significantly reduced. The model is compared with NanoMOS TCAD simulation data and shows a good behavior for temperatures down to 75 K and good agreement for channel lengths from 6 nm to 10 nm. Additionally, the model shows the electron density for the source and drain contacts at different energies.**

I. Introduction

Over the past years, the MOSFET has become smaller and more technologically advanced. Nowadays, the investigated channel length gets down below 10 nm and brings source-to-drain (SD) tunneling effects to light (see Fig. 1). Because SD tunneling leads to a significant increase of the devices off-current, the channel length is physically limited [1], [2], [3]. The non-equilibrium Green's function (NEGF) formalism inherently includes the quantum mechanical and SD tunneling effects and is used to calculate the current in ultra-short channel devices. Therefore, the NEGF formalism has become one of the most promising methods to consider short-channel effects in numerical TCAD device simulators [4], [5], [6], [7]. In order to convert this numerical device simulations to numerically efficient compact transistor models for circuit simulation, a change from iteratively solving Poisson and transport solvers into a straightforward calculation is necessary (see Fig. 2).

In this work the analysis focuses on a DG MOSFET as shown in Figure 3. The source and drain regions are highly n-doped whereas the channel stays intrinsic. For an increased influence on the channel region, the gate dielectric consists of a high-κ oxide material with a dielectric constant $\epsilon_{ox} = 16 \cdot \epsilon_0$. Due to a channel thickness of $t_{ch} = 1$ to $2\,\mathrm{nm}$ and a channel length down to $l_{ch} = 6\,\mathrm{nm}$, a ballistic current transport in the channel is assumed.

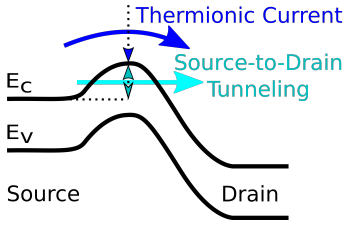

Figure 1. Thermionic current and SD tunneling [2].

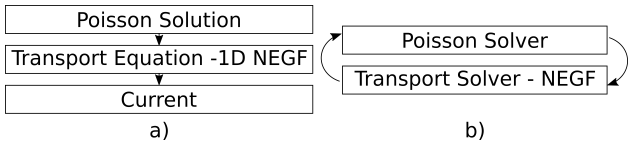

Figure 2. Flowchart of a) the new compact NEGF model and b) common numerical NEGF models.

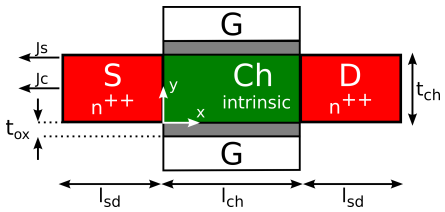

Figure 3. Geometry of a DG MOSFET, showing the doping profiles, structural parameters and the 1D current density at specific y-positions: J_s at the surface and J_c at the center.

II. Model Derivation

In this section the semi-analytical model of the DG MOSFET is introduced. First, the focus lays on the subthreshold region of the device, hence mobile charges may be neglected in the solution of Poisson's equation. The approach is based on an closed-form electrostatics solution for the whole device including the source and drain region [8]. Based on the potential solution the band structure can be calculated for different geometry- and material variations. The Green's function $G(E) = \left[EI - H_L - \Sigma_1 - \Sigma_2\right]^{-1}$, leads to the electron density and hence to the current density for a specific energy level [9]. In order to improve the calculation time of the model, the number of current density calculations

and the accompanying Green's function needs to be reduced from hundreds to a few calculations. Therefore, the current density is only calculated at some specific energy levels and is approximated as shown in Fig. 4. The resulting 1D current densities are calculated two times, one at the channel surface and the other at the channel center. Using mathematical functions, the current density gets integrated from gate to gate in order to calculate the drain current. The good agreement of the model with TCAD simulation data is shown in Fig. 5.

III. Conclusion

In this paper a semi-analytical approach for the calculation of the ballistic current in DG MOSFETs is introduced, which combines the NEGF formalism and a 2D analytical closed-form potential model. The model is implemented in MATLAB and shows a good agreement with the TCAD simulation data for transistors with ultra-short channel lengths down to 6 nm and an ultra-thin body of 1 nm and 2 nm. The effect of dominating source-to-drain tunneling in the off-state of the device results in a subthreshold slope, which is nearly independent from the temperature of the device (see Fig. 6). The model correctly predicts this effect, because it inherently includes thermionic emission and SD tunneling. A variation of channel length and thickness confirms a good scalability of the modeling approach. The integration of the current density by using 18 significant energy levels leads to a notable drop in calculation time. Using a standard laptop computer and applying these mathematical simplifications, the transfer characteristics shown in Fig. 5 are computed at 75 bias steps in less than 10 s.

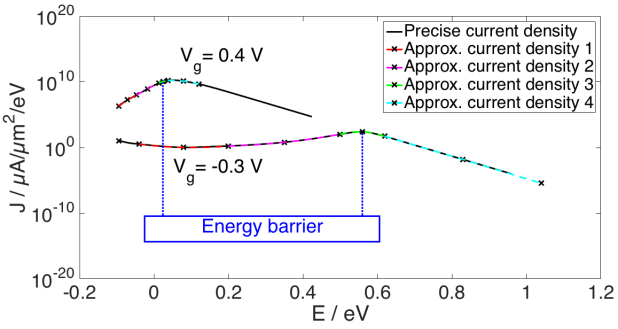

Figure 4. Surface current density at the energy levels for $l_{ch} = 10\,\mathrm{nm}$ and $t_{ch} = 2\,\mathrm{nm}$ at $V_g = -0.3\,\mathrm{V}$ and $V_g = 0.4\,\mathrm{V}$. The precise current density is calculated at each energy level.The approx. current density shows the current density as it is approximated by the mathematical functions, which are defined by the current densities calculated only at positions marked by an "x".

Acknowledgments

This work is supported by the German Federal Ministry of Education and Research (No.03FH001I3). We would like to thank Keysight Technologies for the license donation of the software IC-CAP and AdMOS GmbH for support.

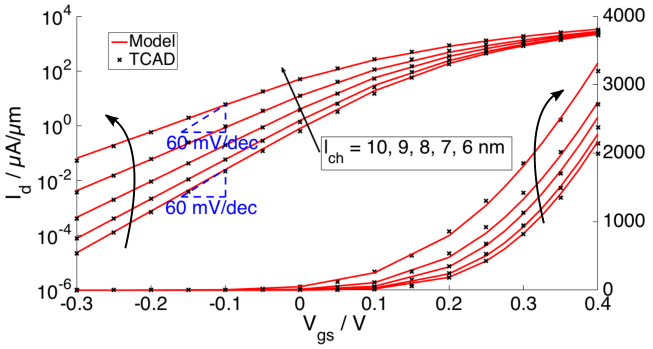

Figure 5. Drain current per gate width for channel geometry of $l_{ch} = 6\,\mathrm{nm}$ to $l_{ch} = 10\,\mathrm{nm}$ and $t_{ch} = 2\,\mathrm{nm}$ at $T = 300\,\mathrm{K}$.

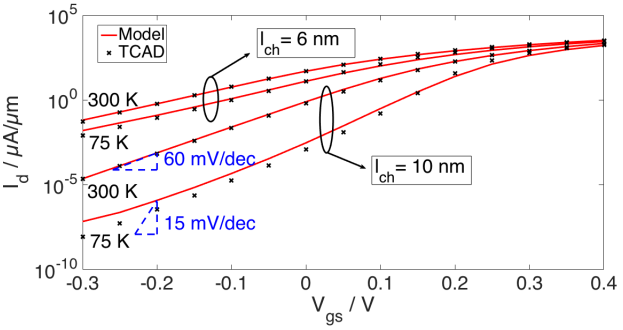

Figure 6. Drain current per gate width for channel geometry of $l_{ch} = 6\,\mathrm{nm}$ and $l_{ch} = 10\,\mathrm{nm}$, $t_{ch} = 2\,\mathrm{nm}$ at $T = 75\,\mathrm{K}$ and $T = 300\,\mathrm{K}$.

References

[1] J. Wang and M. Lundstrom, "Does Source-to-Drain Tunneling Limit the Ultimate Scaling of MOSFETs?." in *Electron Devices Meeting, 2002. IEDM '02. International*, pp. 707–710, Dec. 2002.

[2] Q. Rafhay, R. Clerc, G. Ghibaudo, and G. Pananakakis, "Impact of source-to-drain tunnelling on the scalability of arbitrary oriented alternative channel material nMOSFETs." *Solid-State Electronics*, vol. 52, no. 10, pp. 1474 – 1481, 2008.

[3] J. Watling, A. Brown, A. Asenov, A. Svizhenko, and M. Anantram, "Simulation of direct source-to-drain tunnelling using the density gradient formalism: Non-Equilibrium Greens Function calibration." in *Simulation of Semiconductor Processes and Devices, 2002. SISPAD 2002. International Conference on*, pp. 267–270, 2002.

[4] Z. Ren, S. Goasguen, A. Matsudaira, S. S. Ahmed, K. Cantley, Y. Liu, Y. Gao, X. Wang, and M. Lundstrom, "NanoMOS." https://nanohub.org/resources/1305, Mar 2016.

[5] G. Fiori and G. Iannaccone, "NanoTCAD ViDES." https://nanohub.org/resources/5116, Sep 2014.

[6] O. Baumgartner and Z. S. et al., *VSP-a quantum-electronic simulation framework*, pp. 701–721. Springer Science+Business Media, 2013.

[7] M. P. Anantram, S. S. Ahmed, A. Svizhenko, D. Kearney, and G. Klimeck, "NanoFET." https://nanohub.org/resources/1090, Mar 2016.

[8] M. Graef, T. Holtij, F. Hain, A. Kloes, and B. Iniguez, "Improved Analytical Potential Modeling in Double-Gate Tunnel-FETs." in *Mixed Design of Integrated Circuits Systems (MIXDES), 2014 Proceedings of the 21st International Conference*, pp. 49–53, June 2014.

[9] S. Datta, "Nanoscale Device Modeling: the Green's Function Method." *Superlattices and Microstructures*, vol. 28, no. 4, pp. 253 – 278, 2000.

Charge transfer and charge recombination processes in hybrid lead halide perovskite solar cells studied via laser pulse generated species life-times

Ilario Gelmetti,[a] and Prof. Emilio Palomares[a,b]

[a] Institute of Chemical Research of Catalonia (ICIQ), The Barcelona Institute of Science and Technology (BIST), Avda. Països Catalans 16, Tarragona, Spain
[b] Catalan Institution for Research and Advanced Studies (ICREA), Passeig Lluís Companys 23, Barcelona, Spain

igelmetti@iciq.es

Abstract

Hybrid lead halide perovskite solar cells have received major attention due to its ease of synthesis and high solar power conversion efficiencies achieved. In my second year of doctorate I will focus on the investigation of fundamental processes occurring in the device, like charge transfer and charge recombination in the bulk and in the interfaces by means of photophysical measurements.

1. Introduction

In my first year of doctorate I explored various materials bearing photovoltaic effect. Using the more promising ones I fabricated and tested full photovoltaic devices. These materials have been: tin sulphide, kesterite, lead sulphide quantum dots, methylammonium lead iodide chloride, mixed methylammonium formammidinium lead iodide bromide. These last two hybrid perovskite materials are the more promising ones both in terms of efficiencies and of ease of fabrication. The scientific community has put great effort in optimization of such material composition and synthesis. Still the core of fundamental processes involved in its amazingly high efficiencies is yet to be unequivocally explained.

2. Photophysical measurements

In my second year of doctorate I'm focusing on the photophysical characterization of the fabricated perovskite solar cells. These measurements consist in observing the time dependence in the nano and micro second scale of various parameters (absorbance, voltage or current) after a perturbation (a laser pulse or a short circuit). Comparing the results obtained from different cells we can rationalize the relation between the electronic properties of different materials and the resulting device efficiency. This will allow for better materials design and interfaces engineering.

3. Solar cells structure under study

Up to now the perovskite solar cells structure which reached a sufficient fabrication tailoring and have been investigated by means of photophysical techniques are: FTO / d-TiO_2 / mp-TiO_2 / MAPIC / Spiro-OMeTAD / (Ag or Au); FTO / d-TiO_2 / MAPIC / Spiro-OMeTAD / Ag; FTO / d-TiO_2 / MAPIC / TAE-1 / Ag (where TAE-1 is an alternative organic hole transporting material); FTO / d-TiO_2 / FAMAPIBr / Spiro-OMeTAD / Ag; FTO /d-TiO_2 / FAMAPIBr / TAE-1 / Ag; ITO / PEDOT:PSS / MAPIC / $PC_{71}BM$ / Ag. The best efficiencies have been achieved with the mixed cation FAMAPIBr reaching 16.5 % efficiencies.

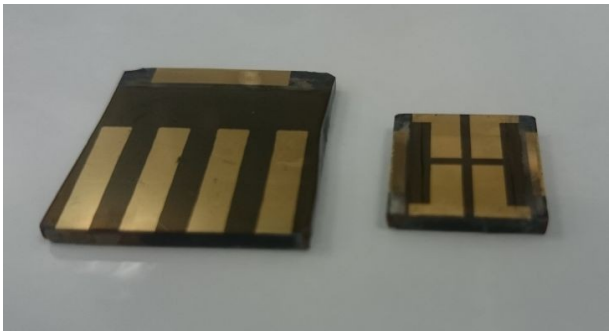

Typical perovskite solar cells with FTO/d-TiO_2/mp-TiO_2/MAPIC/Spiro-OMeTAD/Au structure.

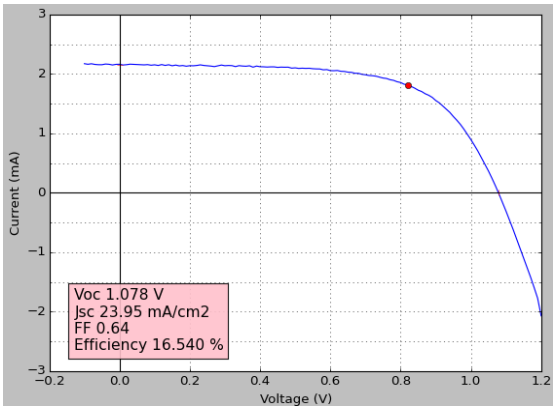

Best efficiency achieved.

Frequency Selective Surface backscatter modulated tag and reader prototype for wearable sensor applications

J. Lorenzo, A. Lázaro, R. Villarino, D. Girbau

Dept. of Electronics, Electrics and Automatic control Engineering, Rovira i Virgili University, Av.Països Catalans 26, 43007 Tarragona, Spain

Abstract

This paper presents a tag based on a modulated frequency selective surface (FSS) as an alternative based on backscattering communication for wearable applications. The tag is composed of an array of dipoles loaded with varactor diodes to modulate the backscatter response. The information is obtained by changing the cross section of the frequency selective surface. The detuning and the power loss of the tag when in contact with the body are studied. Several FSS with different number of dipoles and placed on different surfaces are studied, as a proof of concept. In addition, a temperature sensor for on-body applications is proposed. The reader is also presented and experimental results are provided.

1. Introduction

A wireless body area network (WBAN) is a wireless network used for communication among sensor nodes operating on, in contact, or close to the human body (for users in lifestyle, assisted living, sports and entertainment applications) [1]. This technology has several challenges. One of these is the overall size and weight of the devices that have to be tailored on the body in order to avoid disturbances in human activity. The proximity of the body may easily reduce the efficiency and detune the antennas [2]. Frequency Selective Surfaces (FSS) are periodic structures that have already been used for various applications such as microwave and optical frequency filters, radar absorbing materials (RAMs) and reflectors [3]. Several approaches have been used to change the transmission frequencies, including PIN diodes [4] or varactors [5]. The authors have recently demonstrated the viability of using modulated FSS for RFID applications using readers based on ultra-wide band (UWB) [6] and frequency modulated continuous wave (FMCW) [7] radars at X band. The originality of this paper lies in its study of modulated FSS to be placed on the body for identification and sensing. The reduction of the RCS due to the proximity of high-loss materials and the detuning of antennas are two key problems that limit the use of wireless identification and sensing devices on the body. This problem is mitigated with the use of modulated FSS as shown in this paper. This paper is structured as follows: the operating principle of the system and the design of the prototypes are presented in section 2. The FSS and the prototypes are characterized in section 3. Finally, section 4 contains our conclusions.

2. FSS modulated tag based

A. System description

Fig.1 shows a block diagram of the proposed system for wearable applications. It consists of a reader and semi-passive tags based on modulated FSS.

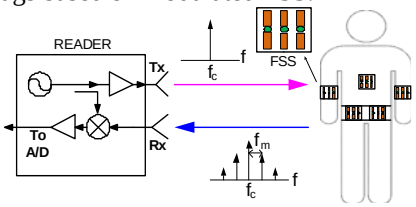

Fig. 1. Block diagram of the system, including the reader and possible locations of FSS.

The transmitter is composed by a generator, with a signal that is amplified to obtain the desired power. A continuous wave (CW) illuminates the tag, which answers by modulating the backscatter of the FSS's RCS. The backscattered signal is demodulated using a homodyne receiver, converted to baseband with a mixer and digitized with an analog to digital converter. A bistatic topology (two antennas, one for transmission and other for reception) is used. A temperature sensor is integrated in the tag, as a proof of concept, which modifies the frequency of a low-frequency oscillator modulating the radar cross section (RCS) of the FSS.

B. On-body modulated FSS

The tag modulates the incident field by switching the varactor diodes that load the FSS's dipoles [7]. The varactor diodes are reverse biased to avoid current consumption. The diodes are switched between 0V and Vcc. When the diodes are biased at 0V (ON state) they present a high capacitance, with the equivalent circuit at microwave regions a short circuit (low impedance state). Whereas the diodes are biased at Vcc (OFF state), the capacitance is considerably lower than in the first case, presenting high impedance at microwave regions. The diodes are therefore ideally equivalent to an open circuit. [7]. The tag is modulated by a f_{tag}. The differential RCS can be expressed as (1). HFSS software is used to simulate the FSS structure. Low-cost silicon varactors from Skyworks SMV1247-079LF are

used and inserted as lumped RLC boundary. The FSS will be implemented using a 100 µm thickness Ultralam 3850 substrate. The structure is simulated on a body human model.

$$RCS_{dif} = \lim_{r\to\infty} 4\pi r^2 \frac{\left|\overline{E}_{S,ON} - \overline{E}_{S,OFF}\right|^2}{\left|\overline{E}_{in}\right|^2} \quad (1)$$

Fig. 2 shows the differential RCS obtained from the difference of the backscattered fields between the ON and OFF states, according to the number of dipoles. This difference is the *RCSdif* (1) when a modulating factor of 1 is assumed. It can be observed that the differential RCS and its bandwidth increase with the number of dipoles, although the maximum of the differential RCS is frequency shifted to lower frequencies. For the fabrication of the prototype, the FSS is connected to a low-frequency oscillator based on the 555 timer configured as astable. The temperature is measured using a negative temperature coefficient (NTC) thermistor (AVX NB20J00472) connected according to the schema in ICM7555 datasheet.

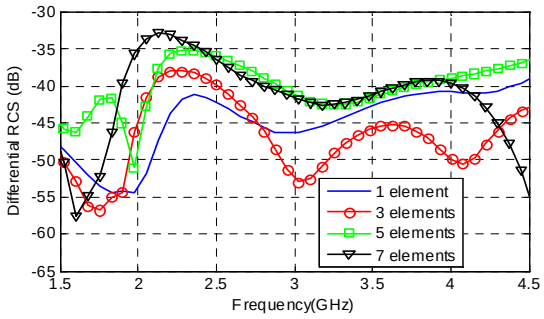

Fig. 2. Simulation of the differential RCS.

3. Measurements and results

From the baseband spectrum obtained from the Fourier transform of the measured signal using the reader at 3 m distance with the tag composed by 7 dipoles in contact with the arm is used: the chirp Z-transform algorithm with a Hamming window is used to achieve the appropriated frequency resolution. A signal-to-noise ratio of about 10 dB is obtained, and that is enough to detect the signal. The temperature is obtained by measuring the frequency of the peak. The sensor is heated with a heat gun and measured while cooling. The NTC resistance (obtained with a multimeter) and the frequency of the peak are measured simultaneously. The temperature of the NTC is obtained from the measured resistance using the calibration curve given by the NTC manufacturer. Fig. 3 shows the relationship between the measured temperature from the calibration curve and the measured modulation frequency for a tag composed by 7 dipoles on the arm. The theoretical model (13-14) is also compared with good agreement. A nearly linear relationship and a correlation coefficient of 98.8% are obtained.

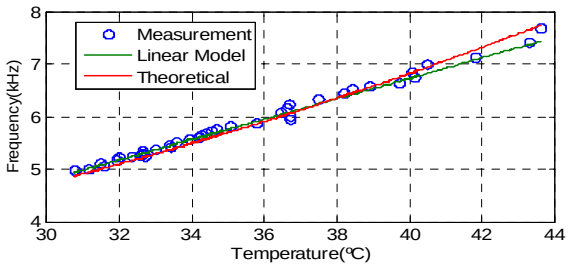

Fig. 3. Detected modulation frequency as function of the NTC temperature for tag composed by 7 dipoles on the arm at a distance of 3 m.

4. Conclusions

This work has studied the feasibility of using modulated frequency surfaces (FSS) for on-body applications. The RCS has been modulated using low-cost reverse-biased varactors. The communication between the tag and the reader is performed by the backscattering technique. The effect of the losses of the body has been investigated both theoretically and experimentally. The problem of multipath interference can be mitigated using spatial diversity techniques or frequency hopping techniques. Read ranges up to 3 m in indoor environments have been obtained. The tag presents low power consumption (60 µA at 3V), which is much lower than other wireless sensors based on transmitters (e.g. a typical Bluetooth 4.0 needs more than 7 mA at 3V during reception or transmission). These results open the door to more complex RFID tags and sensors based on FSS for on-body applications which integrate microcontrollers and more sophisticated sensors depending on the application.

References

[1] E. Monton, J. F. Hernandez, J. M. Blasco, T. Herve, J. Micallef, I. Grech, A. Brincat, and V. Traver, "Body area network for wireless patient monitoring," *IET Communications*, vol. 2, no. 2, pp. 215–222, Feb. 2008.

[2] A. Baroni, H. Rogier, and P. Nepa, "Wearable active Sierpinski fractal antenna for off-body communication," in *2015 IEEE-APS Topical Conference on Antennas and Propagation in Wireless Communications (APWC)*, 2015, pp. 642–645.

[3] B.A. Munk, *Frequency selective surfaces*. New York: Wiley, 2000.

[4] A. Tennant and B. Chambers, "Adaptive radar absorbing structure with PIN diode controlled active frequency selective surface," *Smart Mater. Struct.*, vol. 13, no. 1, p. 122, 2004.

[5] C. Mias, "Varactor-tunable frequency selective surface with resistive-lumped-element biasing grids," *IEEE Microwave and Wireless Components Letters*, vol. 15, no. 9, pp. 570–572, Sep. 2005.

[6] A. Lazaro, A. Ramos, D. Girbau, and R. Villarino, "A Novel UWB RFID Tag Using Active Frequency Selective Surface," *IEEE Transactions on Antennas and Propagation*, vol. 61, no. 3, pp. 1155–1165, Mar. 2013.

[7] D. Girbau, A. Lazaro, J. Lorenzo, and R. Villarino, "Backscatter Transponder Based on Frequency Selective Surface for FMCW Radar Applications," Jun. 2014.

Photo-induced charge kinetics of $MAPbI_3$ vs $FAPbI_3$ perovskite solar cells

J.Jiménez-López[a], L. Cabau[a], E. Palomares[a,b]

[a]Institute of Chemical Research of Catalonia (ICIQ), The Barcelona Institute of Science and Technology (BIST), Tarragona, E-43007, Spain
[b]Catalan Institution for Research and Advanced Studies (ICREA), Barcelona, E-08010, Spain
email: epalomares@iciq.es
Phone +34 977920200 (Ext. 134)

Abstract

Photo-induced charge dynamics of different hybrid organic-inorganic perovskite solar cells have been studied. We have focused on the change of the organic moieties (methylammonium iodide or formamidinium iodide) to see how the charge dynamics change for a better understanding of these devices.

1. Introduction

Hybrid lead halide materials, which present perovskite structure (ABX_3), are widely studied as solar cells due to its excelent photovoltaic properties. Currently, these materials have arranged efficiencies above 20%[1,2].

Methylammonium iodide (MAI) is commonly used as organic precursor for lead halide perovskite[3,4]. Recently, formamidinium iodide (FAI) has been used as precursor, obtaining better values of power conversion efficiency (PCE)[2,5]. To obtain a material capable to absorb in a wider range of the solar spectrum, mixtures of organic precursors and anions have been also used, as $FA_{1-x}MA_xPbI_{3-y}Br_y$, which holds the current PCE record[1].

One of the key factors in order to improve the efficiency of the solar cells is to understand the charge dynamics, which means, to know how many charges are generated, its lifetime or understand how the charges recombine.

As one of the most common precursors used, we have studied methylammonium lead iodide ($MAPbI_3$) solar cells and it has been compared with formamidinium lead iodide solar cells ($FAPbI_3$) and $FA_{1-x}MA_xPbI_{3-y}Br_y$ to study how kinetics differs with the change of precursors.

2. Discussion

We have prepared perovskite solar cells using methylammonium ($MAPbI_3$) and formamidinium ($FAPbI_3$) as the A cation in ABX_3 perovskite structure. Also, it has been prepared a mixture of A and X ions $FA_{1-x}MA_xPbI_{3-y}Br_y$. With these different devices, we have obtained similar J-V curves, with efficiencies about 14 %. For a better comparison, we have used devices with similar efficiency instead of using the best devices obtained.

Then, kinetic dynamics were studied for these devices. The study of charge dynamics is a characteristic matter in our research group. For this purpose, we use different homemade techniques, widely used for OPV and DSSC in our group[6-8]. One of these systems is Photo-Induced Charge Extraction (PICE) that allows the measurement of the carrier density at a given light bias (solar cell voltage produced by continuous white illumination) and Photo-induced Transient Photovoltage (PIT-PV) is useful to correlate the V_{oc} transient with the carrier recombination dynamics.

When we compare PICE and PIT-PV measured at 1 Sun (100 mW/cm^2) we have observed that charge dynamics from every device are different. In $MAPbI_3$, PIT-PV is faster than PICE, which means that the recombination rate is faster than extraction of the charge generated. A biexponential behavior is observed in the PIT-PV decay; this suggests that two types of recombination occur in $MAPbI_3$ devices.

Another approach to measure the carrier density is needed; we have used Photo-Induced Differential Charging (PIDC) that allows the calculation of the charges that can be extracted before recombination takes place.

On the other hand, $FAPbI_3$ and $FA_{1-x}MA_xPbI_{3-y}Br_y$ solar cells present different behavior, PICE and PIT-PV are similar for $FAPbI_3$ while with mixed cations the PICE is faster. In both cases, the charge extraction is faster than the recombination.

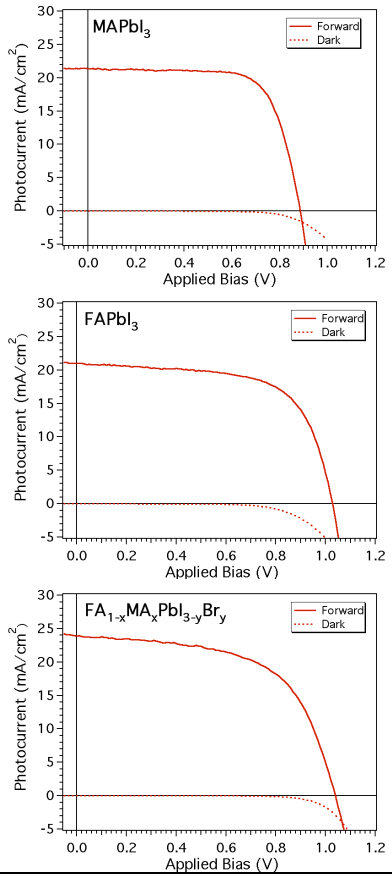

	V_{oc} (mV)	J_{sc} (mA·cm^{-2})	FF (%)	PCE (%)
$MAPbI_3$	885	21.4	71.4	13.5
$FAPbI_3$	1030	21.0	65.0	14.0
$FA_{1-x}MA_xPbI_{3-y}Br_y$	1039	23.9	58.9	14.4

Fig. 1. J-V curves under 1 sun-simulated 1.5 AM (100 mW/cm^2) conditions of the studied devices; Table 1 shows the characteristic parameters obtained.

4. Conclusions

From the comparison between PICE and PIT-PV we conclude that the charge extraction is similar or faster than the recombination for $FAPbI_3$ and $FA_{1-x}MA_xPbI_{3-y}Br_y$ solar cells, while in $MAPbI_3$ solar cells is the opposite, the recombination is faster than the charge extraction. For this reason, PIDC measurements are required to estimate the charge in $MAPbI_3$, and this calculation is not necessary in the case of $FAPbI_3$ and $FA_{1-x}MA_xPbI_{3-y}Br_y$.

Also, the slow decay contribution observed for $MAPbI_3$ have made us think about different factors that affect to the device, as it could be a full coverage of the perovskite over the TiO_2. This is a matter of study in our group.

References

(1) Bi, D.; Tress, W.; Dar, M. I.; Gao, P.; Luo, J.; Renevier, C. m.; Schenk, K.; Abate, A.; Giordano, F.; Correa Baena, J.-P.; Decoppet, J.-D.; Zakeeruddin, S. M.; Nazeeruddin, M. K.; Grätzel, M.; Hagfeldt, A. Science Advances 2016, 2.
(2) Yang, W. S.; Noh, J. H.; Jeon, N. J.; Kim, Y. C.; Ryu, S.; Seo, J.; Seok, S. I. Science 2015, 348, 1234.
(3) Green, M. A.; Ho-Baillie, A.; Snaith, H. J. Nat Photon 2014, 8, 506.
(4) Mali, S. S.; Shim, C. S.; Patil, P. S.; Hong, C. K. Materials Today 2015, 18, 172.
(5) Jeon, N. J.; Noh, J. H.; Yang, W. S.; Kim, Y. C.; Ryu, S.; Seo, J.; Seok, S. I. Nature 2015, 517, 476.
(6) Zewdu, T.; Clifford, J. N.; Hernandez, J. P.; Palomares, E. Energy & Environmental Science 2011, 4, 4633.
(7) Cabau, L.; Vijay Kumar, C.; Moncho, A.; Clifford, J. N.; Lopez, N.; Palomares, E. Energy & Environmental Science 2015, 8, 1368.
(8) Montcada, N. F.; Dominguez, R.; Pelado, B.; Cruz, P. d. l.; Palomares, E.; Langa, F. Journal of Materials Chemistry A 2015, 3, 11340.

Fabrication, Characterization and Stability Analysis of Inverted Polymer Solar Cells

J. G. Sánchez[a], V. S. Balderrama[b], M. Estrada[b], E. Osorio[a], J. Ferré-Borrull[a], L.F. Marsal[a*] and J. Pallarès[a*]

[a]Departament d'Enginyeria Electrònica Elèctrica i Automàtica Universitat Rovira i Virgili

Av. Països Catalans 26, 43007 Tarragona, Spain

[b]Centro de Investigación y de Estudios Avanzados del Instituto Politécnico Nacional (CINVESTAV-I.P.N)

Av. Instituto Politécnico Nacional 2508, 07360 Ciudad de México, México

Abstract

In order to be commercialized, Polymer solar cells have to offer high efficiency and long-term stability to environment. In this paper we present a long-term stability PSCs based on PTB7:$PC_{70}BM$ with inverted architecture, using Titanium oxide (TiO_x) as electron transport layer. Titanium oxide interlayer was deposited by spin-coating technique from a Titanium precursor solution synthesized by sol-gel process. The iPSCs stability was analyzed under three different conditions: encapsulated, air and nitrogen. As expected, devices exposed to air showed a very poor lifetime. Although the stability was improved by using encapsulation process, the lifetime of iPSCs under air conditions still is lower for commercialization. On the other hand, the lifetime of devices under nitrogen conditions was 1200 times higher than air conditions.

1. Introduction

During the last years, Bulk Heterojunction (BHJ) Polymer Solar Cells (PSCs) have attracted much attention in the renewable energy sources field, because of their ability to be easily manufactured on flexible substrates, lightweight, large effective areas with low production costs.[1] Moreover, their power conversion efficiency (PCE) has been rapid increased up to 10% through the improvement of the electrical and optical properties of the electron donor polymer material.[2] These features place the PSCs as a promising technology for low-cost energy production. Besides high efficiency, a long-term stability to environment is required for reach the PSCs commercialization. Conventional PSCs are mainly fabricated with Calcium (Ca) as low-work-function metal and poly(3,4-ethylene dioxythiophene):poly-(styrenesulfonate) (PEDOT:PSS) as hole transport layer. Nevertheless, the easy oxidation of Ca in air presence and the hygroscopic nature of PEDOT:PSS lead to degradation of the active layer and the indium tin oxide (ITO) electrode resulting in poor stability to environment.[3] Recently, PSCs with inverted structure (iPSCs) have been developed in order to improve devices stability. In iPSCs, transition metal oxides such molybdenum oxide (MoO_3) or vanadium oxide (V_2O_5) are mainly used as hole transport layer, because their high work-functions permit obtain low resistance ohmic contacts.[4] Moreover, Titanium oxide (TiO_x) and Zinc oxide are the main materials used as electron-collecting and hole-blocking layer, because of they offer good transparency, high stability and electron mobility as thin films.[5]

In this work we present the fabrication and characterization of high efficiency PSCs with the inverted structure ITO/TiOx/PTB7:$PC_{70}BM$/V_2O_5/Ag. Furthermore, the stability iPSCs was analyzed under three different conditions: Nitrogen, encapsulated and air.

2. Experimental and Results

Figure 1 shows the inverted BHJ Polymer solar cell structure fabricated in this work. TiO_x was prepared via sol-gel methods as showed in [6]. The starting materials were IV titanium isopropoxide (2 mL), 2-methoxyethanol (10 mL), ethanolamine (1 mL). Materials were mixed in a hermetically sealed recipient, inside a glove box and stirred during 3 h at 120 ºC. In order to obtain a TiO_x layer with thickness about 20 nm, TiO_x sol was diluted in anhydrous methanol with ratio 1:6 v/v. The blend was fabricated in N_2 atmosphere, mixing in a bottle PTB7 and $PC_{70}BM$ with the ratio 1:1.5 (w/w), dissolving the blend in chlorobenzene. Blend solution was left stirring by 18 h and left 48 h to aging. ITO-coated glass substrates were cleaned with detergent, ultra-sonicated in acetone, methanol and isopropanol and dried in an oven at 120°C for 20 min. Afterwards, ITOs were exposed to UV during 15 min to eliminate organic materials on their surface. Diluted

TiO_x sol was spin-cast in air on top of the ITO substrates. In order to convert the precursor in TiO_x by hydrolysis, samples were left in ambient conditions during 1 hour and heated at 400 °C increasing the temperature at a heating rate of 20 °C min^{-1}. Subsequently, a blend solution of PTB7:$PC_{70}BM$ was deposited on top of TiO_x layer by spin coating at 800 rpm for 30 s to obtain an active layer with thickness of about 100 nm. Finally, the samples were transferred to a vacuum chamber, where 5 nm of V_2O_5 and 100 nm of Ag were thermally evaporated on the photoactive layer at $6x10^{-7}$ mbar. The active area in both structures was 9 mm^2. Figure 2 shows the current density-voltage J-V characteristics of TiO_x-iPSCs with 100 and 80% of PCE for three different conditions (encapsulated, air and nitrogen) measured under simulated AM 1.5G illumination. As shown in Figure 2, iPSCs encapsulated and exposed to air shown a similar decrease trend of J_{SC} and V_{OC}. On the other hand, iPSCs under nitrogen atmosphere a J_{SC} reduction, whereas V_{OC} variation is no noted. Table 1 shows the normalized values of performance parameters and the lifetime of iPSCs with 80% PCE under three different conditions. As shown in Table 1, all devices showed a slight decrease of V_{OC} and J_{SC}, whereas their FF decreases about 15%. Although the normalized performance parameters of iPSCs with 80% PCE are similar between them, the lifetime are not comparable. Devices under nitrogen atmosphere have long-term stability, while devices under air conditions shown a very poor stability.

3. Conclusions

Stability of iPSCs based on PTB7:$PC_{70}BM$ was analysed under three different conditions: Encapsulated, air and nitrogen. The iPSCs under nitrogen condition reach the 80% of their PCE after 6000h. On the other hand, under air atmosphere the reach the 80% after only 5 h. These results demonstrate that oxygen and water level in air conditions degrade very fast the devices. Although encapsulation reduces the affections caused by oxygen and water, the encapsulated devices reach the 80% PCE after 150 h. In order to improve iPSCs stability toward their commercialization, an efficient encapsulation process have to be used, considering that the lifetime expected will be not higher than the lifetime of devices under nitrogen conditions (6000 h).

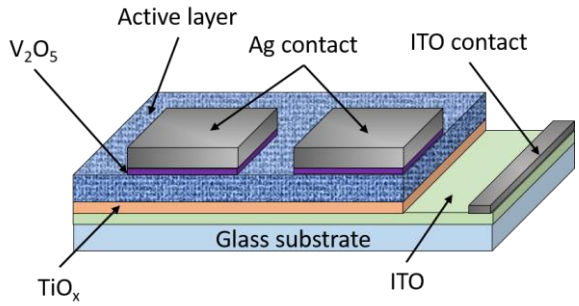

Figure. 1 Inverted and standard structures of BHJ-PSCs fabricated.

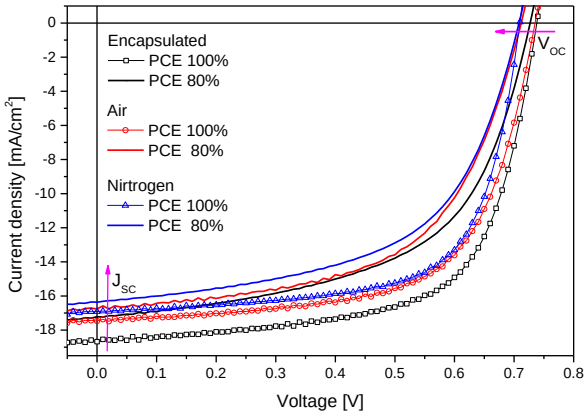

Figure 2. J-V characteristics of iPSCs illuminated by AM 1.5G irradiation under three different conditions: encapsulated, air and nitrogen with 100 and 80 % of PCE.

Parameter	Encap.	Air	Nitrogen
V_{OC}	0.98	0.96	0.99
J_{SC}	0.92	0.96	0.97
FF	0.86	0.88	0.84
Lifetime [h]	148	5	6070

Table 1. Lifetime and normalized performance parameters of iPSCs with 80% of PCE.

Acknowledgements

This work was supported by the Spanish Ministry of Economy and competitiveness (MINECO) under grant number, TEC2015-71324-R by the ICREA under the ICREA Academia Award, by Catalan authority under project AGAUR 2014 SGR 1344 and CONACYT Project 237213 in Mexico.

References

[1] V. S. Balderrama, F. Avila-herrera, J. G. Sánchez, J. Pallarès, O. Vigil-Galán, L. F. Marsal and M. Estrada, IEEE Journal of Photovoltaics, vol. 6, pp. 1–7, 2016.

[2] Z. He, B. Xiao, F. Liu, H. Wu, Y. Yang, S. Xiao, C. Wang, T. P. Russell, and Y. Cao, Nat. Photonics, vol. 9, no. 3, pp. 174–179, 2015.

[3] V. S. Balderrama, M. Estrada, P. L. Han, P. Granero, J. Pallarés, J. Ferré-Borrull, and L. F. Marsal, Sol. Energy Mater. Sol. Cells, vol. 125, pp. 155–163, 2014.

[4] J. Meyer, S. Hamwi, M. Kröger, W. Kowalsky, T. Riedl, and A. Kahn, Adv. Mater., vol. 24, no. 40, pp. 5408–5427, 2012.

[5] S. Yuan, Y. Zhang, W. Liu, and W. Zhang, Electrochim. Acta, vol. 116, pp. 442–446, 2014.

[6] C. Meneses, J. G. Sanchez, M. Estrada, A. Cerdeira, J. Pallarés, B. Iñiguez, and L. F. Marsal, Microelectron. Reliab. vol. 54, no. 5, pp. 893–898, 2014.

Fabrication and characterization of Rugate Filters based on Nanoporous Anodic Alumina

L. Karen Acosta, Elisabet Xifré-Perez, Josep Ferré-Borrull, and Lluis F. Marsal*

Departament d'Enginyeria Electrònica, Elèctrica i Automàtica, Universitat Rovira i Virgili, Avinguda Països Catalans 26, 43007 Tarragona, Spain; Phone: 977 55 85 24
***Email: lluis.marsal@urv.cat**

Abstract

In this work, we present a study of the design parameters for sinusoidal-anodization rugate filters made of nanoporous anodic alumina (NAA). The galvanostatic control of the anodization provides an accurate control of the porosity and growth rate of the alumina. Our study establishes the principles for understanding the effect of the fabrication parameters (current amplitude, offset current, period length and number of periods) on the optical properties of the sinusoidal rugate filters. The obtained results reveal that reflection spectrum of the rugate filters can be precisely tuned in the UV, visible and IR range by adjusting the different fabrication parameters.

1. Introduction

Optical properties of nanoporous anodic alumina (NAA) are interesting many photonic applications. Such optical properties can be modified in several ways [1] and applications such as optical biosensing have already been demonstrated [2]. One interesting optical application is the development of rugate filters: a multilayer structure with continuous variation of refractive index along the pore. It can be produced in a quasi-galvanostatic regime with a sinusoidal perturbation of the current and leads to structures with a sharp stop band around the design wavelength. One advantage of such structures is the possibility to overlap several sinusoidal profiles resulting in several tunable stop bands in the same structure. This feature permit to envision other applications such as colorimetric sensing or barcode labeling.

2. Materials and Methods

Materials

Aluminum (Al) foil thickness = 250 µm and purity = 99.999%), Oxalic acid ($C_2H_2O_4$), ethanol (C_2H_5OH), acetone ($(CH_3)_2$ CO), perchloric acid ($HClO_4$), hydrochloric acid (HCl), copper chloride ($CuCl_2$), double deionized water (DI)

Fabrication

First Al substrates were degreased in acetone, cleaned with ethanol and DI water and finally dried under steam of air. Before the anodization, Al substrates were electropolished in a mixture of Ethanol and Perchloric acid 4:1 at 20 V and 5ºC for 5 min. During the electropolishing step the stirring direction was alternated every 60 s. After the electropolishing the samples were cleaned with ethanol and DI water and dried under steam of air [3]. Then, the anodization was carried out in $H_2C_2O_4$ 0.3 M at 5ºC applying a sinusoidal current profile with several design parameters like offset current (Io), amplitude current (I1), Period (T) and number of periods (N). Figure 1 shows the sinusoidal current profile. In this work, we performed 6 different samples. Table 1 shows their different parameters of fabrication.

Table 1. Fabrication Parameters

Sample ID	I_0 (mA)	I_1 (mA)	T (s)	N
R1	4	2	150	100
R2	3	2	150	100
R3	4	2	200	100
R4	4	1	150	100
R5	4	2	100	100
R6	4	2	150	200

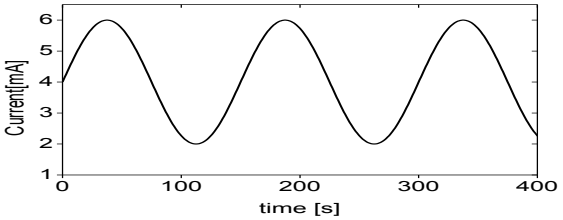

Figure 1. Sinusoidal current profile of anodization step

3. Results

Figure 2 shows the reflectance spectrum of the 6 samples. R1 (T=150s), R3 (T= 200s) and R5 (T=100s) can be compared as they have different period lengths. We can observe that the longer the anodization period the longer the wavelength of the R peak (shift to the red). For the case of different offset current (I_0) samples (R1 with I_0=4 mA and R2 with I_0=3 mA), we can observe that when I0 is higher the wavelength of R peak increases. Furthermore when changing the amplitude current I_1 (samples R1 with I_1=2 mA and R4 with I_1=1 mA), R peak is placed at the same wavelength position but the height decreases when the I_1 is lower. Finally if we analyzed the influence of the number of periods (samples R1 with N=100 and R6 with N=200) a slightly shift to the left (UV range) is observed.

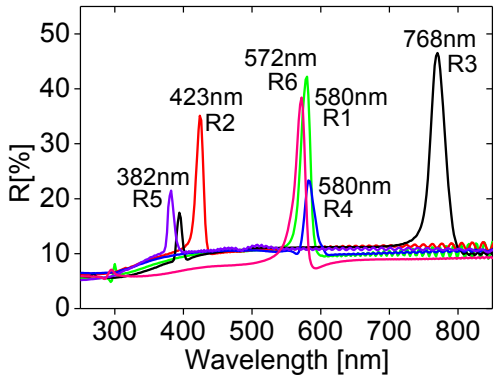

Figure 2. Reflectance spectra of nanoporous anodic alumina rugate filters of the 6 samples with different parameters.

7. Conclusions

Rugate filters were fabricated applying a sinusoidal current profile with different fabrication parameters in order to study their influence in the wavelength peak. Each parameter has a different influence on the resultant reflectance spectra. The offset current and the period tune the wavelength position of the peak , the amplitude current contributes to the height and width of the peak and finally the number of periods induces a slightly shift that could be ascribed to a small porosity gradient in depth.

Summarizing, the fabrication parameters (N, T, I_0 and I_1) not only determine the position of the wavelength peak but also contribute to their height and width.

References

[1] J. Ferre-Borrull, E. Xifre-Perez, J. Pallares, L.F. Marsal. Optical properties of nanoporous anodic alumina and derived applications. In: D. Losic, A. Santos editors. Nanoporous Alumina. Fabrication, Structure, Properties and Applications, Springer Series in Materials Science Vol. 219 (2015) p. 185-217.

[2] G. Macias, L.P. Hernández-Eguía, J. Ferré-Borrull, J. Pallares, L.F. Marsal, ACS Appl. Mater. Interfaces, **5** (2013) 8093.

[3] G. Macias, J. Ferré-Borrull, J. Pallares, L.F. Marsal, Nanoscale research letters, 9 (2014) p. 315

Stimuli-responsive drug release using Nanoporous Anodic Alumina coated with layer by layer polyelectrolyte deposition

M.Porta-i-Batalla, C.Eckstein, P.Formentín, J Ferré-Borrull, L.F.Marsal

Departemant d'Enginyeria Electrònica, Elèctrica i Automática, ETSE, Universitat Rovira i Virgili, Avda. Països Catalans 26, 43007 Tarragona, Spain

*Corresponding author. Tel: 977 55 85 24 E-mail:maria.porta@urv.cat

Abstract

Controlled drug-delivery systems (DDS) are an encouraging solution to some drug disadvantages such as reduced solubility, deprived biodistribution, tissue damage, fast breakdown of the drug, cytotoxicity or side effects. Self-ordered Nanoporous Anodic Alumina is an auspicious material for drug delivery due to its biocompatibility, stability and controllable pore geometry. Its use in drug delivery applications has been explored in several fields, including: therapeutic devices for bone and dental tissue engineering, coronary stent implants and carriers for transplanted cells. In this work, we have created and analysed a stimuli-responsive drug-delivery system based on layer by layer (LbL) pH-responsive polyelectrolytes and nanoporous anodic alumina. The results demonstrate that is possible to use control the drug release using a polyelectrolyte multilayer coating that will act as a gate.

1. Introduction

Some studies have been already performed in the drug delivery framework using porous materials [1][2]. Nanoporous anodic alumina (NAA) is one of the most attractive material for drug delivery applications due to the pore size and depth of NAA can easily be controlled by regulating the anodizing voltage, time and electrolyte composite. The use of these material is aimed to locate organic molecules (drugs) on biomaterials the application of which is to reconstruct or regenerate living tissues, deal with infections, inflammation (consequence of chirurgical implantation) or just for drug constant administration. Drug depots in human body with controlled and retained release are able to improve quality of life and assist long-term treatments; in addition the development of those new and more efficient drug delivery systems solve conventional drug therapy problems related to limited drug solubility, lack of selectivity and unfavourable pharmacokinetics. The drug release from porous materials is based on molecular diffusion from the pores, and it is mainly governed by the pore dimensions. Therefore, adjustment of pore diameter and pore depth has been considered a common strategy to control drug release performance.
In this study NAA platforms with pore diameters of 80 nm and pore depth of 15 μm were used as model porous material. In order to realize a controlled drug release, a pH stimuli responsive polyelectrolyte LbL assembly has been used to coat the porous matrixes. The effect of pH in the drug release kinetics has been studied and discussed.

2. Experimental Section

Nanoporous alumina anodization
Ordered nanoporous anodic alumina was prepared by the two-step anodization method. Perchloric acid and phosphoric acid were used as electrolytes for electropolishing and anodization respectively. Aluminum plates were degreased in acetone and ethanol to eliminate organic impurities. They were then subsequently electropolished in a mixed solvent of perchloric acid and ethanol (1:3) at a constant applied voltage of 20 V for 6 min. To suppress breakdown effects and to enable uniform oxide film growth at high voltage (194 V in phosphoric acid) a protective layer at lower voltage (174 V in phosphoric acid) was performed for 180 min. After this pre-anodization, a ramp of 0,05V/s was used to reach the hard voltage (194 V) during 24h. Then, after this first step, the porous alumina grown on the aluminum surface was removed by a wet chemical etching in a mixture of phosphoric acid (0,4 M) and chromic acid (0,2 M) (1:1 volume ratio) at 70ºC. The second anodization step was performed under the same experimental conditions (194 V) as they were used in the first step in order to obtain ordered nanoporous alumina. 15 μm porous depths were achieved controlling the total charge on the second step [3]. The morphologies of the NAA substrates were characterized by Environmental Scanning Electron Microscopy (ESEM).

Polyelectrolytes assembly

In order to cover the nanopore walls with polyelectrolyte layers, nanoporous anodic alumina was coated with 3-aminopropyl triethoxysilane (APTES). The positively charged APTES substrates would allow negatively charged polyelectrolytes to be attached on the substrate. For LbL deposition, the NAA substrates were immersed consecutively into negative charged solution of poly(styrenesulfonate) (PSS, 1 mg/ml in 5 mM CaCl2 in deionized water), and positive charged solution of poly(allyl amine) (PAH, 1 mg/ml in 5 mM CaCl2 in deionized water), alternating risings with deionized water. Dipping times in polyelectrolyte solutions were 30 minutes and the washing step in deionized water lasted for 10 min. All the steps were repeated for 5 times [4] (Fig.1).

Drug loading and release studies

Positively charged doxorubicin hydrochloride (DOX) was selected as a model drug. LbL-NAA samples were immersed in 1 mg/ml DOX solution at pH = 2 in the dark at room temperature overnight. Then the DOX solution was adjusted to pH = 8 and the samples were stirred 2 hours in the dark.

Drug release was monitored by drug photoluminescence over 6000 minutes. Once we reached 4560 minutes the pH 7.2 medium was changed for pH 5.4 medium. The photoluminescence measurements were taken on a fluorescence spectrophotometer with a Xe lamp used as the excitation light source at room temperature and an excitation wavelength (λex) of 480 nm. Results are shown in Fig. 2.

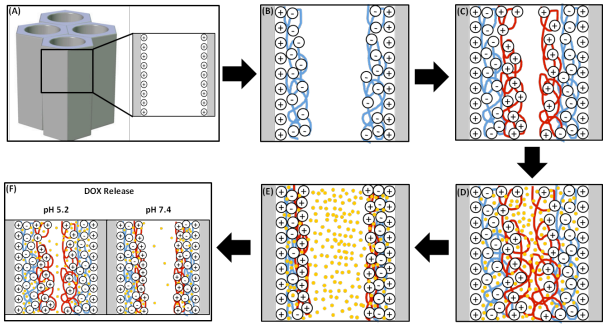

Fig. 1. Schematic representation of the polyelectrolyte layer-by-layer deposition procedure. B) PSS deposition by immersing the APTES treated surface. C) PAH deposition by immersing the PSS covered substrate. D) DOX loading in the swollen PEM film at pH 2.0 E) DOX confinement due to the PEM layer contraction at pH 8.0 F) DOX releases at different pH media.

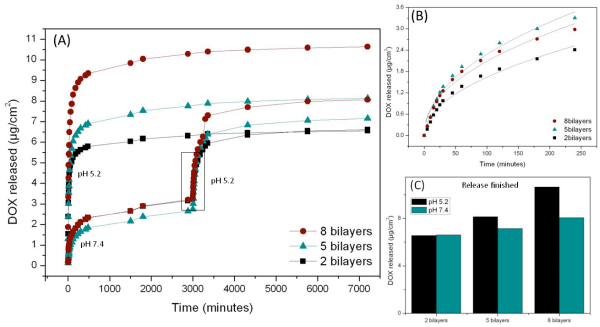

Fig. 2. Complete release profiles of DOX from NAA coated with different polyelectrolyte bilayer numbers at pH 5.2 and 7.4. with different burst releases framed. B) Nonlinear fitting for the second burst release at pH 5.2. C) Total DOX amount released for every different sample during the monitoring.

3. Conclusions

In this study we have demonstrated that nanoporous anodic alumina and LbL polyelectrolytes can be used as a stimuli-responsive drug-delivery system. We reported the ability of NAA platforms to be used as drug controlled release reservoir. DOX loaded LbL-NAA in vitro release profile was established for different pH medium and changes on those profiles have been testified. Results show that LbL-NAA has potential applications in local drug delivery.

Acknowledgements

This work is supported in part by the Spanish Ministry of Economy and competitiveness TEC2012-34397, the Catalan authority AGAUR 2014SGR1344, ICREA under the ICREA Academia Award.

References

[1] D.-H. Kwak, J.-B. Yoo, and D. J. Kim, "Drug Release Behavior from Nanoporous Anodic Aluminum Oxide," J. Nanosci. Nanotechnol., vol. 10, no. 1, pp. 345–348, Jan. 2010.

[2] H.-J. Kang, D. J. Kim, S.-J. Park, J.-B. Yoo, and Y. S. Ryu, "Controlled drug release using nanoporous anodic aluminum oxide on stent," Thin Solid Films, vol. 515, no. 12, pp. 5184–5187, Apr. 2007.

[3] A. Santos, J. Ferré-Borrull, J. Pallarès, and L. F. Marsal, "Hierarchical nanoporous anodic alumina templates by asymmetric two-step anodization," Phys. Status Solidi Appl. Mater. Sci., vol. 208, no. 3, pp. 668–674, 2011.

[4] M. L. Bruening, D. M. Dotzauer, P. Jain, L. Ouyang, and G. L. Baker, "Creation of Functional Membranes Using Polyelectrolyte Multilayers and Polymer Brushes," Langmuir, no. 18, pp. 7663–7673, 2008.

Analytical Approach to Consider Gaussian Junction Profiles in Compact Models of Tunnel-FETs

Michael Graef[1,2,✠], Fabian Hosenfeld[1,2], Fabian Horst[1,2], Atieh Farokhnejad[1,2], Benjamín Iñíguez[2] and Alexander Kloes[1]
[1]Competence Centre for Nanotechnology and Photonics, Technische Hochschule Mittelhessen, Giessen, Germany
[2]DEEEA, Universitat Rovira i Virgili, Tarragona, Spain
✠michael.graef@ei.thm.de

***Abstract*—The impact of Gaussian-shaped doping-profiles on the potential and the current transfer characteristics of an Double-Gate (DG) Tunnel-FET (TFET) is investigated in this paper. Based on results of the analysis, a simple model by solving Poisson's equation is developed. The model is able to calculate the potential difference in the channel region caused by the applied doping gradient. Considering the modifications in the two-dimensional (2D) potential profile the band-to-band (B2B) tunneling current is calculated with help of Wentzel-Kramers-Brillouin (WKB) approximation and Landauer transmission theory. The results are validated by comparison with TCAD simulation data.**

***Index Terms*—1D Poisson, 2D Potential, Analytical Modeling, Gaussian Doping Profile, Double-Gate (DG) Tunnel-FET.**

I. Introduction

In the past years the Tunnel-FET has become one of the most promising candidates to be successor of the standard MOSFET technology. Due to its B2B tunneling current transport mechanism it is able to overcome the physically limited subthreshold slope (S) of MOSFETs ($\frac{60mV}{dec}$) caused by the drift-diffusion transport [1]. Recently fabricated devices show a minimum S down to 40 $\frac{mV}{dec}$ [1]. For introduction of the Tunnel-FET in one of the next technology nodes the research community still has to face some difficulties limiting the device performance. The suppression of trap-assisted-tunneling (TAT) is required, which causes an increased OFF-state current and decreases S. For a high ON current an abrupt junction at the source tunneling barrier is necessary but technologically difficult to achieve. Therefore, in this paper an extensive analysis is done to investigate the impact of the steepness of the doping profile on the electrostatics and the device current. The outcome of this analysis is used to develop a simple stand-alone model that is able to consider doping profiles by calculating a potential difference between an abrupt and a non-abrupt profile at the tunneling barrier. By including the new approach in our previously published current model [2] a comparison of the potential difference and the current transfer characteristics with TCAD simulation data is achieved.

II. Model Derivation

In this work the analysis focuses on a DG n-Tunnel-FET as shown in Fig. 1. The source region is highly p-doped, the channel stays intrinsic and the drain region has a reduced n-doping to suppress the ambipolar current and reach an optimized I_{ON}/I_{OFF} ratio [1]. For an increased influence on the channel region, the gate dielectric consists of the high-κ material HfO_2 with a dielectric constant $\epsilon_{ox} = 25{\cdot}\epsilon_0$. Quantum effects can be neglected for the calculations since the channel thickness is at least 10 nm [3].

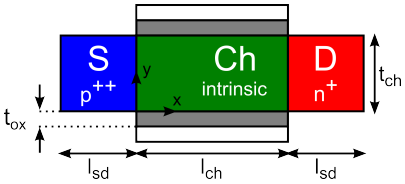

Figure 1. Device geometry of a DG n-Tunnel-FET, showing its structural parameters.

In the following steps, the derivation of the model is focused on the doping profile at the source-to-channel junction of the device. The results are easily transferable to the drain side. The first step is the definition of a doping profile for the simulation, which is set to a realistic Gaussian shaped type (see Fig. 2).

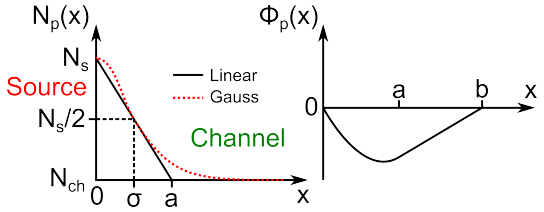

Figure 2. Gaussian-shaped (red dots) and linear (black line) doping profile at the source-to-channel junction, showing the standard deviation σ and model parameters a, b. Schematic potential difference calculated by the model.

In the model the doping profile is assumed to be linear, with the variables a, b (see Fig. 2). In order to find the potential solution the Poisson's equation is decomposed to

$$\Delta\widetilde{\phi} = -\frac{\varrho(x)}{\epsilon} = \Delta\phi + \Delta\phi_p \tag{1}$$

with the potential for non-ideal ($\widetilde{\phi}$) and ideal (ϕ) doping profile, respectively, and the potential difference $\phi_p = \widetilde{\phi} - \phi$, whereby $\Delta\phi_p = -q \cdot N_p(x)/\epsilon$. With the linear doping profile $N_p(0 \leq x \leq a) = N_s(a-x)/a$ the Poisson's equation can be solved assuming the electric field and the potential to be continuous over the channel length. Therefore, the potential difference for $0 \leq x \leq a$ is given through

$$\phi_p(x) = -\frac{q \cdot N_s}{\epsilon \cdot a}\left(\frac{a}{2} \cdot x^2 - \frac{1}{6} \cdot x^3\right) + E_p(0) \cdot x \tag{2}$$

and for $a < x \leq b$ by

$$\phi_p(x) = \phi(a) - \left(\frac{q \cdot N_s}{2 \cdot \epsilon} \cdot a - E_p(0) \right) (x - a), \qquad (3)$$

with the electrical field $E_p(0) = q \cdot N_s/(\epsilon \cdot b) \cdot (ab/2 - a^2/6)$. Due to the 2D influence of the gate electrode on the channel region the closer the additional dopants Np(x) are to the gate dielectric the more they are under control of the gate. The analysis for the DG Tunnel-FET showed, that this effect can be captured by coupling the parameter a with the σ of the profile and add a dependency to position y in the channel:

$$a \approx -\frac{\sigma \cdot (c_1 - 1)}{(t_{ch}/2)^4} \cdot (y - t_{ch}/2)^4 + c_1 \cdot \sigma, \qquad (4)$$

with $1 < c_1 < 1.5$. The analysis also showed a dependency between the channel/oxide thickness and b

$$b \approx t_{ch} \cdot \pi/4 + \widetilde{t}_{ox} \qquad (5)$$

with the scaled oxide thickness $\widetilde{t}_{ox} = t_{ox} \cdot \epsilon_{ch}/\epsilon_{ox}$. To capture the last effect a shifting of the potential difference is needed in order to properly model the additional potential drop in the source region. Therefore, stands $\Phi_p(x) = \phi_p(x - x_{shift})$.

III. Model Verification

A meaningful parameter describing the quality of a doping profile is the standard deviation σ. Therefore, the electrostatics of the device should be strongly dependent on this parameter. Figure 3 illustrates the potential difference for various standard deviations at the y cross section close to the gate dielectric ($y = 0.05$ nm) in comparison of TCAD simulation data.

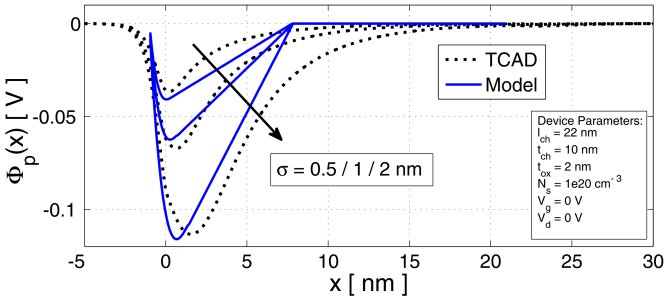

Figure 3. Shifted potential difference Φ_p for various standard deviations, with $x_{shift} = -1$ nm and $\sigma_{model} = 0.7 \cdot \sigma - x_{shift}$.

The model predicts the basic influence of the standard deviation and is able to estimate the resulting potential difference. As mentioned before, the influence of the gate electrodes on the channel region should result in a major dependency of the potential difference on the position y in the channel. Figure 4 shows a comparison of the model with the TCAD simulation data. In the end, the model is able to predict the impact of the standard deviation on the potential profile including the influence of the gate. Therefore, we are able to include the model in our previous work [2] and compare the current transfer characteristics for various standard deviations. Fig. 5 depicts a good match between the model and the current from TCAD data. Increased deviations between model and TCAD for low V_g are not of interest because under these conditions leakage mechanisms such as e.g. TAT, which were not taken into account, limit the minimum current. It is important to note that for all plots the model parameters were kept constant. Therefore, the model can accurately predict the influence of the doping profile's steepness on the transfer characteristics.

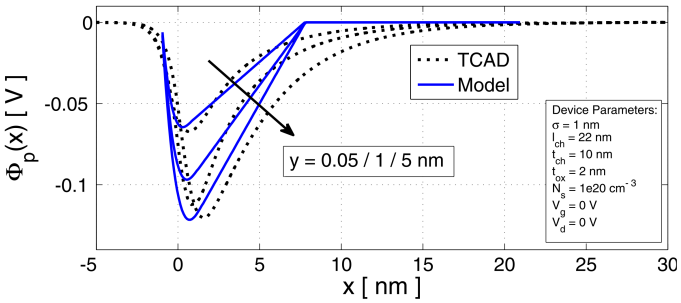

Figure 4. Shifted potential difference Φ_p for various positions y, with $x_{shift} = -1$ nm and $\sigma_{model} = 0.7 \cdot \sigma - x_{shift}$.

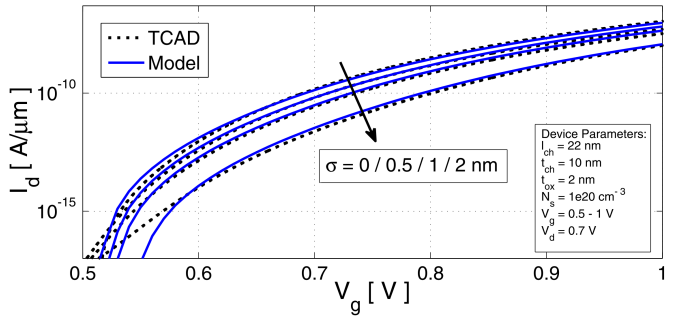

Figure 5. Current transfer characteristics for various standard deviations, with $x_{shift} = -0.5$ nm, $\sigma_{model} = 0.7 \cdot \sigma - x_{shift}$ and $b = 17$ nm.

IV. Conclusion

In this paper a simple model is presented to catch the potential difference caused by Gaussian-shaped doping profiles at the tunnel junction by solving the Poisson's equation. It is able to predict the influence of the steepness of the profile on the electrostatics and the ON current of the device. By integrating the model in our previous work a comparison of current transfer characteristics in DG-Tunnel-FETs is in good agreement.

V. Acknowledgment

This project was supported by the German Federal Ministry of Education and Research under contract No.1779X09, by German Research Foundation (DFG) under Grant KL 1042/3-1, and by the European Commission under FP7 Project IAPP-218255 ("COMON").

References

[1] A. Seabaugh and Q. Zhang, "Low-Voltage Tunnel Transistors for Beyond CMOS Logic." *Proceedings of the IEEE*, vol. 98, pp. 2095 –2110, dec. 2010.

[2] M. Graef, T. Holtij, F. Hain, A. Kloes, and B. Iníguez, "A 2D closed form model for the electrostatics in hetero-junction double-gate tunnel-FETs for calculation of band-to-band tunneling current." *Microelectronics Journal*, vol. 45, no. 9, pp. 1144 – 1153, 2014.

[3] Y. Omura, S. Horiguchi, M. Tabe, and K. Kishi, "Quantum-Mechanical Effects on the Threshold Voltage of Ultrathin-SOI nMOSFETs." *IEEE Electron Device Letters*, vol. 14, no. 12, pp. 569–571, 1993.

The Flyback Converter as DC-DC Transformer for PV Balancing

*Md. Nazmul Hasan, Luis Martínez-Salamero, Carlos Olalla

*Graduate Student
Group of Automatic Control and Industrial Electronics
Dept. of Electrical, Electronics and Automatic Control Engineering, Universitat Rovira i Virgili
Contact info: mdnazmul.hasan@urv.cat

Abstract

This paper reviews the analysis, design and realization of a low power flyback converter for differential power processing (DPP) in photovoltaic (PV) systems. The operation of the flyback converter in discontinuous conduction mode (DCM) has been analyzed and an appropriate coupled inductor has been designed. The advantages and limitations of the converter in this application have been verified with experimental measurements.

1. Introduction

A Photovoltaic (PV) system usually consists of a series arrangement of PV modules containing series-connected PV cells. This series connection of PV cells forces the same current through the entire string and it causes losses in presence of mismatch. Typically bypass diodes are used to avoid cell failure due to hot spot spots which can be induced by power losses on reverse-biased cells operating in breakdown [1]. However, bypass diodes produce power losses in presence of mismatch, hence the overall efficiency of the PV system is reduced. Several full power processing (FPP) [2], [3] and differential power processing (DPP) [4], [5] methods have been proposed to overcome this problem. The DPP approach only requires the processing of the differential power among the different PV portions, while FPP requires the processing of the total power in the PV system. In consequence, DPP architectures can employ converters with reduced power rating, while they also achieve higher overall efficiency. This paper reviews the realization of a flyback converter for the DPP isolated-port architecture (shown in Fig. 1) introduced in [5] and evaluates its advantages and drawbacks.

2. Operation of the Flyback Converter

The power converters employed in the isolated-port architecture require: (i) bidirectional power transfer, (ii) input-output galvanic isolation and (iii) input-output voltage conversion ratio equal to 1. The flyback converter (shown in Fig. 2) features these characteristics. Given that the converters in the isolated-port architecture typically process low power [5], DCM operation of the flyback converter is assumed. Moreover, DCM results in simple control design and dynamic behavior, while allowing quick change in the power flow direction. The waveforms of the flyback converter operating in DCM can be seen in Fig. 3.

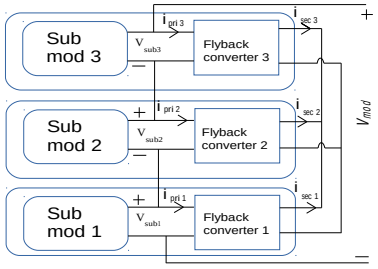

Fig. 1 DPP isolated-port architecture in [5].

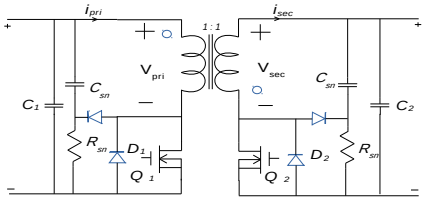

Fig. 2 Schematic of the bidirectional flyback converter.

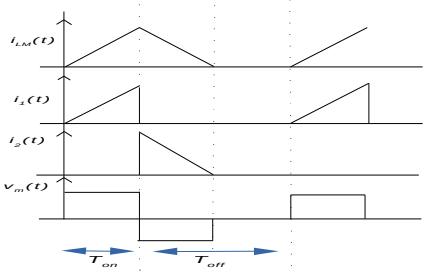

Fig. 3 Waveforms of flyback converter in DCM.

3. Design the Flyback Converter

One of the key aspects in the design of the flyback converter is to obtain the magnetizing inductance (L_M) such that the converter always operates in DCM. Considering i_{LM} as the current of the primary magnetizing inductance of the transformer, Vg as the input voltage, D as the duty cycle and Ts as the switching frequency of the converter, from Fig. 4, the average value of input current i_1 is:

$$\langle i_1 \rangle = \frac{V_g . D^2 . T_s}{2L_M} \qquad (1)$$

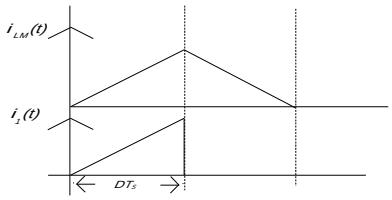

Fig. 4 Waveforms of the magnetizing inductance and input currents at maximum power, i.e., in the boundary between DCM and CCM.

Thus, in order to operate in DCM, the maximum value of L_M is as follows

$$L_M \leq \frac{V_g . D^2 . T_s}{2.\langle i_1 \rangle} \qquad (2)$$

For an output power of 25 W, input and output voltages of 10 V (D=0.5), and a switching frequency of 50 kHz, from equation (2) the magnetizing inductance must be equal or less than 10 µH. In addition to satisfying the requirements of the magnetizing inductance, it is very important to achieve high coupling coefficient, reducing the leakage inductance in the transformer as much as possible. A high leakage inductance causes high voltage spikes across drain-to-source of the MOSFET during turn-off, and this may damage the device permanently. Hence, in the prototype, the primary and secondary windings have been wrapped together and kept as close as possible to the core, with no bobbin-former. Measurements of the parameters of the resulting transformer, shown in Table 1, show a coupling coefficient of 0.98.

Inductance (µH)	Coupling coefficient	Leakage ind. (µH)	Airgap (mm)	# of turns
9.81	0.981	0.18	0.68	5

Table1. Experimental measurements of the parameters of the transformer (ETD-34 core, Strand diameter 0.32mm, equivalent AWG#19)

4. Experimental Results

This section presents the experimental results of the flyback converter. The measurements were done with an input voltage of 10 V. The load was varied in order to get different output powers and the duty cycle was modified in order to obtain 10 V at the output. It can be seen from Fig. 5 that the converter efficiency is in the range of 80-90 % and that

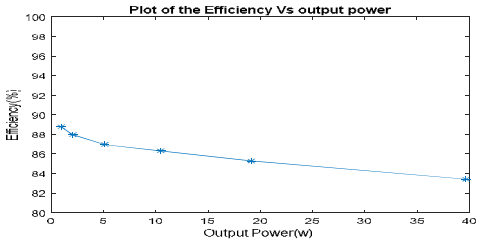

Fig. 5 Efficiency vs. Output power.

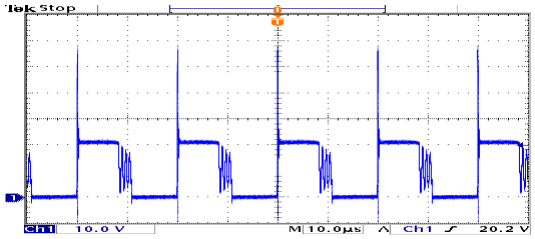

Fig. 6 The drain-to-source voltage exhibits a voltage peak of 60 V due to the leakage inductance (Pin=20 W, D=0.45).

efficiency decreases with increasing operating power. Figure 6 shows the drain-to-source voltage of the MOSFET when the input power is 20 W. The voltage spike at the beginning of T_{off} due to the leakage inductance of the transformer exhibits a considerable peak of approximately 60 V, even in presence of the RC snubber circuit

5. Conclusion

This paper reviews the realization of a flyback converter for DPP in PV systems and evaluates its performance with experimental measurements from a prototype. While the main advantage of the converter is the low part count, several drawbacks limit its efficiency and reliability. First, the leakage inductance produces undesired voltage stress in the MOSFETS, such that snubber circuits leading to power loss must be employed. In addition, losses in the diode during Toff also affect the efficiency negatively. Efficiency results show, however, high copper losses which may be related to a high AC resistance of the transformer windings. Improved Litz wires or copper foils may be used in the future to improve the efficiency of the power stage.

References

[1] J. Wohlgemuth and W. Herrmann, "Hot spot tests for crystalline siliconmodules," in Proc. IEEE Photovoltaic Spec. Conf., Jan. 2005, pp. 1062–1063.

[2] JG. Walker and P. Sernia, "Cascaded DC-DC converter connection of photovoltaic modules," *IEEE Trans. on Power* Electron. vol. 19, no. 4,pp. 1130–1139, 2004.

[3] S. Poshtkouhi, A. Biswas, and O. Trescases, "DC-DC converter for high granularity, sub-string MPPT in photovoltaic applications using a virtual parallel connection," in *Proc. IEEE Appl. Power Electron. Conf. andExpo.*, Feb. 2012, pp. 86–92.

[4] J. T. Stauth, M. D. Seeman, and K. Kesarwani, "Resonant switched capacitor converters for sub-module distributed photovoltaic power management," *IEEE Trans. on Power Electron.*, vol. 28, no. 3, pp. 1189–1198, 2013.

[5] C. Olalla, M. Rodriguez, D. Clement, and D. Maksimovic, "Architectures and control of submodule integrated DC-DC converters for photovoltaic applications," *EEE Trans. on Power Electron.*, vol. 28,no. 6, pp. 2980–2997, 2012.

Mass spectrometry imaging in metabolomics using sputtered gold nanolayers

Pere Ràfols[1], Dídac Vilalta[1,2], Sònia Torres[1], Raul Calavia[1], Jesús Brezmes[1,2], Oscar Yanes[1,2,3], Noelia Ramírez[1,2] and Xavier Correig[1,2]

[1] Department of Electronic Engineering, Rovira i Virgili University, IISPV, Avinguda Països Catalans 26, 43007 Tarragona, Spain;
[2] Spanish Biomedical Research Centre in Diabetes and Associated Metabolic Disorders (CIBERDEM), C/ Monforte de Lemos 3-5, 28029 Madrid, Spain;
[3] Centre for Omic Sciences (COS), Rovira i Virgili University, Avinguda Universitat 3, 43204 Reus, Spain;

Abstract

Mass spectrometry imaging (MSI) is a molecular histology technique that maps the distribution of molecules in biological tissues with high spatial resolution. The most widely used MSI technique is Matrix Assisted Laser Desorption/Ionization (MALDI), but some organic matrices used in classical MALDI may impact the quality of the molecular images due to limited lateral resolution and strong background noise in the low mass range, hindering its use in metabolomics. Here we present a matrix-free LDI technique based on the deposition by sputtering of gold nanolayers on tissue sections. This gold coating method is quick, fully automated and repetitive and allowed growing highly controlled nanolayers, necessary for high quality and high resolution MS image acquisition. The performance of the developed method has been tested on the acquisition of MS images of various tissues including brain. These results, together with the reliable MS spectrum calibration using gold peaks, make the developed method a valuable alternative to classical organic matrices for MSI applications.

1. Introduction

Classical histology, which allows the visual inspection of stained tissue sections and the identification of specific regions, has been largely used as an essential tool in medical diagnosis. However, histology is not capable of determining the chemical composition of those tissue regions and must be complemented with other techniques to achieve molecular identification, requiring additional sample preparation steps and analysis. In the recent years, mass spectrometry imaging (MSI) has emerged as a straightforward alternative [1]. MSI, also called molecular histology, consists in the acquisition of molecular images of biological tissue sections, providing the chemical information directly from the tissue.

The most widely used ionization technique in MSI is Matrix Assisted Laser Desorption Ionization (MALDI) [2], where an organic matrix is applied over thin tissue sections to promote the desorption/ionization of the proteins, lipids and other metabolites. Classical matrix application techniques may produce compound diffusion, deteriorating the lateral resolution of the image, and/or inhomogeneities during deposition over the tissue. To overcome these problems, matrix sublimation has recently been introduced as matrix deposition technique allowing high spatial resolutions. Nevertheless, one of the main drawbacks of MALDI is that the organic matrices introduce a considerable number of MS signals in the low m/z range of the spectrum (below 1000 Da). These signals interfere severely with the MS peaks of the low weight compounds, making their application to metabolomics studies a challenging task.

A recent application has used sputtering deposition of silver for the MSI of olefins from tissue sections [3]. This study demonstrated the viability of sputter depositions for MSI metabolomics applications, with high spatial resolution. Furthermore, the characteristic silver peaks and clusters can be used for internal mass calibration along the different m/z regions of the obtained spectrum.

Hence, in this study we present the application of gold nanolayers deposited by sputtering to obtain metabolomics MS images of animal tissues by LDI-MS. In comparison with silver, gold has only one stable isotope, thus reducing the number of background peaks and facilitating the detection of trace compounds and provides highly stable nanolayers.

2. Methods

Tissues were sliced into 10 μm sections using a cryostat and directly placed on indium tin oxide (ITO)-coated glass slides. Next, a 5 nm layer of gold nanoparticles was deposited over the tissue using a sputtering system running in RF mode. The MS spectra were acquired with a Bruker UltrafleXtreme MALDI-TOF instrument. The instrument has been adjusted with a raster step down to 10 μm, a total accumulation of 500 laser shots per pixel, a laser frequency of 2 kHz and a laser attenuation of 50%. After the acquisition, data was exported to XMASS format and converted to a custom format to perform data processing using in-house developed software.

3. Gold nanolayer optimization

The sputtered deposition of the gold nanoparticles has been optimized to achieve the highest MS signal intensities at the lowest laser power fluencies. The gold nanolayer deposited over the tissue must provide enough gold nanoparticles to promote the desorption/ionization of the metabolites, but it has to be thin enough to enable the laser to reach the tissue-gold interface. Moreover, the deposited gold nanolayer must ensure the correct identification of the gold MS peaks to guarantee the reliability of the spectrum mass calibration using these peaks as an internal reference.

Various gold layer deposition conditions were used to acquire MS data from animal tissues. The data obtained with each of the tested gold layers were compared to determine the optimal gold coating conditions. In order to provide an objective comparison criterion between different sputtering conditions, we have calculated three parameters from the average spectrum of each gold layer: the total ion count (TIC) defined as the summing up intensities of all MS peaks; the peak count defined as the total number of detected MS peaks; and the fragmentation ratio calculated by dividing the intensity of the head group fragment of the phosphatidylcholines (m/z 184.07) by the sum of intensities of the MS peaks found in the 700 to 900 Da m/z range. Taking into account these three parameters plus the detectability of gold peaks we chose an approximately 5 nm thick layer as the most reliable for MSI application.

4. MSI of animal tissues

The viability of the optimized gold nanolayers for metabolomics MSI applications by LDI-MS was checked by acquiring MS images of different animal model tissue sections achieving lateral resolutions down to 10 µm. In order to not compromise sensibility, for this study, C57/BL mouse brain tissue was acquired with raster sizes of 80 µm that has been previously reported to provide enough resolution to represent the tissue structures in these organs.

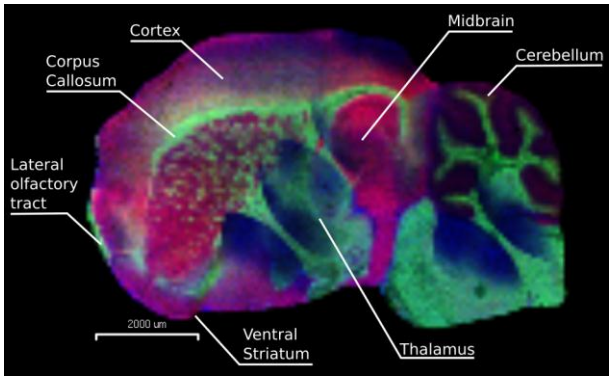

Fig.1. Sagittal section of a mouse brain acquired with the optimized sputtered gold layer at a raster size of 80 µm. Relative abundance of three ions found to reproduce the brain morphology (m/z 845.45, 849.64 and 213.04) are displayed encoded in RGB code where each ion concentration is related with red, green and blue colors respectively.

Figure 1 shows the MS images of three selected ions (m/z 845.45, m/z 849.64 and m/z 213.04) obtained from the sagittal section of a mouse brain. These three ions have been encoded with a RGB color system (m/z 845.45 in red, m/z 849.64 in green and m/z 213.04 in blue) to provide an accurate representation of brain morphology where different brain sections can be even more clearly distinguished and labeled. The reliability of the developed MSI method was confirmed by comparing the brain morphology obtained with the MS images with a consecutive brain slice stained with Hematoxilyn. Moreover, ions m/z 845.45 and 849.64 were putatively identified as the potassium adducts of two lipids commonly found in brain tissues.

5. Conclusions

In this study we present the development of an alternative method for the acquisition of MS images based on the sputter deposition of gold nanolayers over thin tissue sections. Gold is a highly stable material and neither degradation nor oxidation occurs after sample preparation or during the LDI-MS acquisition. The presented sample preparation method is fast, fully automated and reproducible. Furthermore, this dry deposition method avoids the delocalization of metabolites in biological tissues improving the spatial resolution of the obtained MS images.

The capacity of gold to acquire a wide range of metabolites has been demonstrated through the acquirement of MS images of various tissues. The mass spectra obtained from the analysed tissues are very rich in the m/z range under 1000 Da. Background MS peaks from gold nanoparticles are just five single signals homogenously distributed across the spectra. These signals have a minimal interference on metabolites detection and can also be used for a reliable spectrum alignment and mass calibration between pixels. Moreover, we have been able to putatively identify various endogen metabolites in brain demonstrating the reliability of the acquired spectra.

References

[1] J. L. Norris and R. M. Caprioli, “Imaging mass spectrometry: a new tool for pathology in a molecular age.” Proteomics. Clin. Appl., vol. 7, no. 11–12, pp. 733–8, Dec. 2013.

[2] Karas, M.; Hillenkamp, F, “Laser desorption ionization of proteins with molecular masses exceeding 10,000 daltons.” Anal. Chem., vol. 60, pp. 2299–2301, 1988.

[3] Dufresne, M.; Thomas, A.; Breault-Turcot, J.; Masson, J.-F.; Chaurand, P. “Silver-Assisted Laser Desorption Ionization For High Spatial Resolution Imaging Mass Spectrometry of Olefins from Thin Tissue Sections.” Anal. Chem. Vol. 85, pp. 3318–3324, 2013

CARATERIZATION OF RHEUMATHOID ARTHRITIS (RA) PATIENS BY ^{1}H-NUCLEAR MAGNETIC RESONANCE SPECTROSCOPY (^{1}H-NMR).

Rocío Fuertes Martín[1], Núria Amigó Grau[1], Joan Carles Vallvé[2], Silvia Paredes[2], Dèlia Taverner[2], Lluis Masana[2]. Xavier Correig Blanchar[3].

[1]Biosfer Teslab,SL; Metabolomics platform, Universitat Rovira i Virgili, IISPV; CIBERDEM; Reus-Tarragona, Spain.
[2]Unitat de Recerca en lipids i arteriosclerosi, Hospital Universitari Sant Joan de Reus; IISPV; CIBERDEM; Reus-Tarragona, Spain.
[3]Metabolomics platform, Universitat Rovira i Virgili, IISPV; CIBERDEM; Reus-Tarragona, Spain.
rfuertes@biosferteslab.com;

Objective:

RA is an autoimmune and chronic inflammatory disease associated with a high index of morbidity and mortality by cardiovascular disease (CVD). ^{1}H-NMR is a technique capable of determining the lipoprotein and glycoprotein profiles, to characterize dyslipidaemias and to estimate the cardiovascular and inflammatory risk.

The objective of this study is to characterize the plasmatic lipoprotein and glycoprotein profiles of RA patients using ^{1}H-NMR in order to identify patterns of the disease's severity.

Material and methods:

Serum samples of 214 RA patients were analysed by ^{1}H-NMR. Lipoproteic (Liposcale® test [1]) and glycoproteic profiles were characterized. A mathematical treatment of the signal was conducted as follows: the raw spectra was fitted with four analytic Lorentzian functions reproducing the peak associated with the glycoproteins (Base, GlycB, GlycA, and GlycL) based on their chemical shift. From each of these functions the total area and height (proportional to the concentration), the position (characteristic of the magnetic environment) and the width (related to the flexibility and the aggregation state of the molecules generating the signal) were determined.

On the other hand, the traditional inflammatory markers such as C-reactive protein (CRP), fibrinogen, glycosylated haemoglobin (HbA1c) and the erythrocyte sedimentation rate (ESR) were also determined.

We used univariate statistical analysis in order to identify the association between the inflammatory markers and the ^{1}H-NMR lipoprotein and glycoprotein profiles and multivariate statistical methods to model their contribution on the index of disease activity (DAS28) categorized by quartiles.

Results:

There was a positive association between HbA1c levels and IDL-cholesterol, IDL-triglycerides and VLDL-triglyceride concentrations. It was also noted that ESR was positively associated with LDL-triglycerides and the index DAS28 was associated with HDL-triglycerides (Table 1).

	IDL-C	*VLDL-TG*	*IDL-TG*	*LDL-TG*	*HDL-TG*	*Total VLDL-P (nmol/L)*	*Large VLDL-P (nmol/L)*	*Medium VLDL-P (nmol/L)*	*Small VLDL-P (nmol/L)*	*LDL-Z*
HbA1c	0.16	0.17	0.17	-	-	0.15	0.15	0.14	0.14	-
ESR	-	-	-	0.15	-	-	-	-	-	-0.16
DAS28	-	-	-	-	0.20	-	-	-	-	-0.19

Table 1: Correlation coefficient of significant values (p<0.005) between lipid variables and HbA1c and DAS28.

Moreover, ESR, CRP and Fibrinogen concentrations were positively associated with parameters of glycoproteins concentration (Table 2).

	ESR	*CRP*	*Fibrinogen*
GlycB-area	0.14	0.14	-
GlycA-area	0.23	0.17	0.17
GlycB-Height	0.27	0.23	0.25
GlycA-Height	0.27	0.20	0.20
GlycB-Height	-	-	-
GlycA-Width	-0.22	-0.20	-0.18
GlycB-Width	-0.38	-	-

Table 2: Correlation coefficient of significant values (p<0.005) between glycoproteins functions and traditional inflammatory markers.

Finally, a partial least squares discriminant analysis (PLSDA) showed that the inclusion of glycoproteins along with traditional parameters of inflammation improves the classification of the activity and severity of RA according to the highest quartile of DAS28 as is shown in Figure 1, where the area under the ROC curve was 0.824.

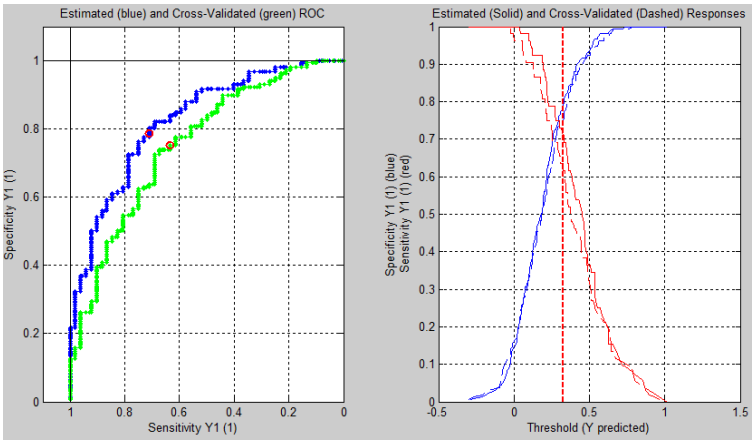

Figure 1: ROC (Receiver Operator Characteristics) curve predicting the behaviour of the model containing the glycoprotein and lipoprotein variables along with the RA traditional parameters of inflammation (CRP, ESR and fibrinogen).
The area under the curve (AUC) of the estimated curve (blue) was 0.824 and the AUC of the Cross-validated curve (green) was 0.754.

Conclusions:

^{1}H-RMN metabolomics is a useful tool to identify atherogenic and inflammatory profiles in patients with RA. These profiles, along with the classic AR inflammatory parameters, provide more accurate information about the severity and activity of the disease.

Keywords: ^{1}H-NMR, metabolomics, lipoproteins, glycoproteins, inflammation.

Acknowledgement:
This research has been subsidized by the Government of Catalonia within the Industrial PhD program.

References

[1] R. Mallol, N. Amigó, M. A. Rodríguez, M. Heras, M. Vinaixa, N. Plana, E. Rock, J. Ribalta, O. Yanes, L. Masana, and X. Correig, "*Liposcale: a novel advanced lipoprotein test based on 2D diffusion-ordered 1H NMR spectroscopy.*," *J. Lipid Res.*, vol. 56, no. 3, pp. 737–46, Mar. 2015.

1H-NMR-based metabolomics: Different “ways” to analyse complex data

R. Barrilero1,2,3* and X. Correig1,2,3

1. Dept. d'Enginyeria Electrònica, Elèctrica i Automàtica, Metabolomics Platform, URV, Tarragona, Spain
2. Institut d'Investigació Sanitària Pere Virgili (IISPV), Reus, Spain
3. Centro de Investigación Biomédica en Red de Diabetes y Enfermedades Metabólicas Asociadas (CIBERDEM), Madrid, Spain
*Corresponding to: ruben.barrilero@urv.cat

Proton nuclear magnetic resonance (1H-NMR) is a leading technique for exploratory stages in metabolomics studies. 1H-NMR of biological samples offers dozens of features and can provide, for instance, an overview of the affected metabolic pathways in group of patients with a disease or under drug treatments. In spite of the advantages that NMR offers compared to other techniques (reproducibility, high-throughput analysis and no sample separation), the analysis of 1H-NMR data is not straightforward since 1H-NMR spectra are subjected to several artifacts (baseline and phase artifacts, signal overlapping, spectral shifts, low S/N …). Extracting information requires therefore applying models based on prior knowledge (when available) or may need of complex data structures (created for example combining a large number of samples or using additional NMR dimensions) in order to exploit the inner data relationships and obtain the physically-meaningful underlying models.

In this presentation, the concept of “ways” refers to the dimensionality of the data being analyzed and will be the unifying thread to introduce the different projects developed during the doctorate. All the projects are framed in the context of the development of computational tools for 1H-NMR data analysis in metabolomics, and a set of multivariate methods are presented to deal with the data structures involved. In the first project, a software tool for profiling lipid extracts was developed. This tool applies curve fitting methods to resolve individual signals in every 1H-NMR spectrum, which can be considered as a one-way array (vector) of 1xN spectral points. In the second project, we improve the quantification of low molecular weight metabolites (LMWM) in serum when they are affected by interactions with proteins. In this biological matrix, every LMWM give two overlapping signals in a 1H-NMR spectrum, one “free” response belonging to the LMWM part that is in the aqueous media and the other one “bound”, which is the part that creates a complex with proteins. Using an extra NMR dimension we create a two-way data array (matrix) for each serum sample, where the individual signals can be separated and quantified using unsupervised curve resolution methods [1]. Using curve resolution also provides additional information about the strength of the binding interactions. The third project consists in the development of generalized regression models to predict standard lipids in serum using 1H-NMR [2]. Models were evaluated using two different data structures. In the first case we used a two-way array MxN sized, where M represents the number of serum samples and N the spectral points. For this data we used conventional PLS regression models. In the second case an extra NMR dimension related with the outcome was included, creating a three-way array (also referred as “box”) for which N-PLS regression models were applied.

References

[1] de Juan, A., J. Jaumot, R. Tauler (2014). Multivariate Curve Resolution (MCR). Solving the mixture analysis problem. Analytical Methods 6, 4964-4976 doi:10.1039/C4AY00571F

[2] Barrilero, R., E. Llobet, R. Mallol, et al. (2015). Design and evaluation of standard lipid prediction models based on 1H-NMR spectroscopy of human serum/plasma samples. Metabolomics 11, 1394-1404 doi:10.1007/s11306-015-0796-5

Parameters Estimation of a Transformer from the Load Test

S. García-Ríos, L. Guasch-Pesquer, F. González-Molina

Group of Industrial Electronics and Automatic Control, Rovira i Virgili University, Tarragona, Spain
email: sara.garcia@urv.cat

Abstract

In this research a methodology is presented in order to estimate the parameters of a linear single-phase transformer model from laboratory tests. Starting with both the estimated parameters from the no-load and short circuit tests and the measurements obtained in different points of the load test, more accurate parameters have been obtained using an iterative algorithm based on the minimum error in the internal voltage drop and the internal electrical power loss. The transformer has been tested on 28 load points using different types of load: resistive (R), inductive (RL) and capacitive (RC) to achieve different power factors and load indexes.

1. Introduction

The transformer is probably one of the most useful electrical devices invented. It can increase or decrease the voltage and current, isolate circuits between them and increase or decrease the apparent value of a capacitor, an inductance or a resistor [1]. Due to its importance in power systems, it has to be studied in detail in order to understand how it actually operates. Many procedures have been developed to obtain the characteristic parameters of transformers [2]. In the first part of this paper, the selected transformer is described, followed by a description of the type of tests run and the algorithm designed, to finalize with the improved calculation of the electrical parameters.

2. Transformer

A. Selected model

The Gamma equivalent circuit of a transformer used is shown in Figure 1, where:

V1: primary voltage
V2': secondary voltage referred to the primary
I1: primary current
I2': secondary current referred to the primary
I0: no-load current
IFe: active component of I0
Iμ: reactive component of I0
Rcc: winding resistance
RFe: resistance associated with the core losses
Xcc: dispersion reactance
Xμ: magnetizing reactance

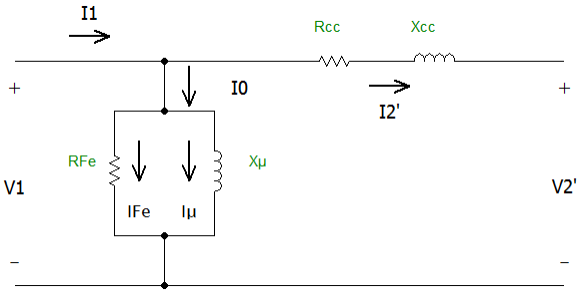

Figure 1. Gamma equivalent circuit of the transformer

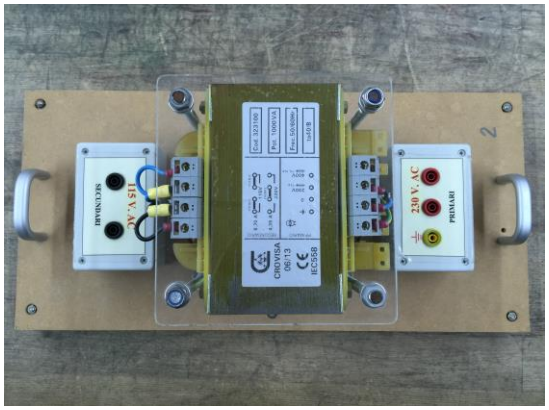

Figure 2. Transformer used in the tests

The values of the secondary are referred to the primary side.

B. Selected transformer

The transformer tested is shown in Figure 2 and its characteristics are shown in Table 1.

3. Methodology

Starting with the estimated parameters from the no-load and short circuit tests and the measurements obtained in 28 points of the load test, more accurate parameters have been obtained using an iterative algorithm based on the minimum error in the internal voltage drop and the internal electrical power loss.

Table 1. Characteristics of the tested transformer

Label	CROVISA
Model	06/13
Power (kVA)	1.00
Number of phases	1
Nominal primary voltage (V)	115
Nominal secondary voltage (V)	230
Nominal primary current (A)	8.70
Nominal secondary current (A)	4.35

Table 2. Initial and final values of Rcc. Xcc and Zcc

	Rcc	**X_{cc}**	**Zcc**
Initial	1.786	0.647	2.018
Final	0.859	0.968	1.121

Table 3. Initial and final errors

	Electrical power losses (%)	**Voltage drop (%)**
Initial	3.49	0.83
Final	0.69	0.47

A. No-load and short-circuit tests

The no-load test was made in order to calculate the values of RFe and Xμ, and the core losses. These results are considered constant in this work.

The short circuit test was made in order to calculate the initial values of the parameters Rcc and Xcc.

B. Load test

A load test was also carried out in 28 points. The loads were designed in order to achieve different values of the power factor ($\cos\varphi_2$) and load index (k) for each type of load (R, RL, RC).

The voltage reference during the tests was the secondary voltage, and it was very close to 230 V. The following characteristics were measured for each tested point: primary voltage (V_1), primary current (I_1), primary active power (P_1), primary reactive power (Q_1), primary apparent power (S_1), power factor in the primary ($\cos\varphi_1$), secondary voltage (V_2), secondary current (I_2), secondary active power (P_2), secondary reactive power (Q_2), secondary apparent power (S_2) and power factor in the secondary ($\cos\varphi_2$).

4. Designed algorithm

The initial values used in the algorithm of the parameters RFe, Xμ, Rcc and Xcc were calculated from the no-load and the short circuit tests. Also, from the no-load test, the core losses PFe were estimated.

Before starting the iteration, the upper and lower limits of R_{cc} and Z_{cc} are defined as Rcc(2), Rcc(3), Zcc(2) and Zcc(3) respectively.

For each iteration the algorithm calculates a value of Rcc(n) and Zcc(n), from the two iteration loops with less error. Using as a reference the real values of

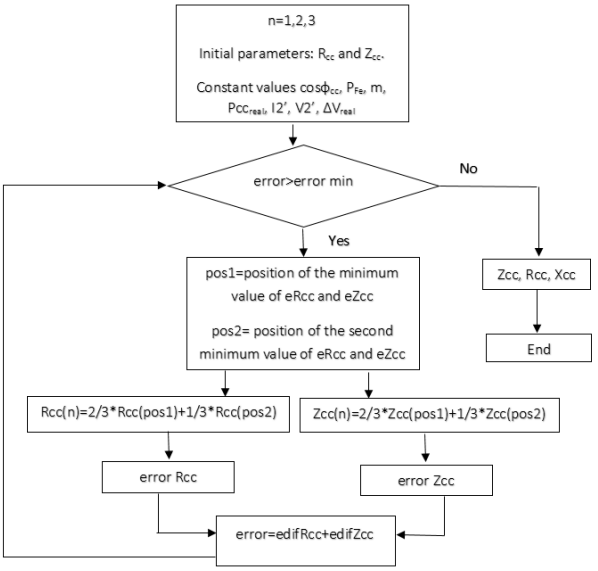

Figure 3. Block diagram of the iteration methodology used to estimate Rcc and Xcc

electrical losses and voltage drop the iteration error is calculated by these new parameters.

A flow chart of algorithm is shown in Figure 3. When the error is minimized, a more accurate value of Z_{cc} and R_{cc} is given, and X_{cc} can be calculated.

5. Results

More accurate parameters are obtained with this algorithm. Table 2 shows the difference between the initial and final values of Rcc, Xcc and Zcc respectively, and Table 3 shows the calculated errors using the parameters of Table 2.

6. Conclusions

It is possible to determine the parameters of a linear single-phase transformer model from laboratory tests by using a designed algorithm that through iteration obtains more accurate parameters than the ones calculated with the no-load and short circuit tests. The errors are reduced and the algorithm used is reliable and effective.

This method has good results, but requires the use of different values and types of loads. This fact is not always possible, in particular with large power transformers.

References

[1] Wildi, T. “Máquinas Eléctricas y Sistemas de Potencia”. 2007.

[2] Meister, D., & De Oliveira, M. A. G. “The use of the Least Squares Method to estimate the model parameters of a transformer”. 2009 10th International Conference on Electrical Power Quality and Utilisation, EPQU’09, 0–5, 2009.

Synthesis of Single Crystalline In_2O_3 octahedra for detecting oxidizing and reducing gases at trace levels

Sergio Roso[a, b], Atsushi Urakawa[b] and Eduard Llobet[a]

[a]Minos-Emas, Universitat Rovira i Virgili, Av. Països Catalans 26, 43007, Tarragona, Spain
[b]Institute of Chemical Research of Catalonia (ICIQ), The Barcelona Institute of Science and Technology. Av. Països Catalans, 16, 43007, Tarragona, Spain

Abstract

Single crystalline indium oxide (In_2O_3) octahedra have been synthesized by means of a vapor phase transport method at high temperature. The gas sensing properties of this material against oxidizing and reducing gases have been examined and the conditions for selectively detecting such gases have been established. A high response towards NO_2 has been obtained at a relatively low operating temperature (i.e., 130ºC). The fact that the response of the nanomaterial is more than two orders of magnitude higher for NO_2 than for H_2, even in the presence of ambient moisture, makes it very promising for the selective detection of oxidizing species (at ppb levels) under real ambient conditions.

1. Introduction

Semiconductor metal oxides have become a major technological drive in the field of gas sensors because of their low cost, high sensitivity, fast response and their relative simplicity. Among others, indium oxide (In_2O_3) is nowadays an interesting material for its unique optical and optoelectronic properties that make it suitable not only for gas sensors but also for solar cells and liquid-crystal displays. In this work, we developed a method to synthesize In_2O_3 octahedra by means of a vapor phase transport method. The structure of the material was characterized and its sensing properties were examined, exhibiting great sensitivity towards low concentration of oxidizing and reducing gases.

2. Experimental

In_2O_3 octahedra were synthesized on top of Si/SiO_2 substrates via a vapor-phase transport method using a horizontal chemical vapor deposition (CVD) furnace. Si/SiO_2 substrates were previously cleaned by sonication. The cleaning process follows three steps of 5 minutes each in acetone, ethanol and deionized water, and then dried in synthetic air. In a typical experimental procedure, 0.3 g of high purity In metal (99.99%) was placed on an alumina boat. Next to it, at a distance of around 1 cm the Si/SiO_2 wafer was placed. Then, the alumina boat with the precursor and the wafer were placed at the center of the horizontal furnace. The temperature was raised to 1000ºC at a rate of 15ºC/min, and kept constant for 120 min. The reaction took place in a dynamic Ar atmosphere (300 mL/min).

After that, the material was removed from the Si/SiO_2 substrate and mixed in a solution of 1,2-propanediol. The resultant ink was used to deposit the material by screen printing on top of an alumina substrate with interdigitated Pt electrodes. At the back side of such substrate, a Pt heater was placed in order to perform gas tests under different temperatures.

3. Results and Discussion

Fig. 1 shows FESEM images of the In_2O_3 octahedra synthesized at 1000ºC. As shown, the final product consists of a high density of octahedral shaped structures (Fig. 1a). No other morphologies are observed, which indicates the uniformity of the process. A regular octahedron is composed of eight equilateral triangles, four of which meet at the same vertex. The side of each triangle is about 500 nm and all the faces are almost perfectly smooth and without any visible structural defects.

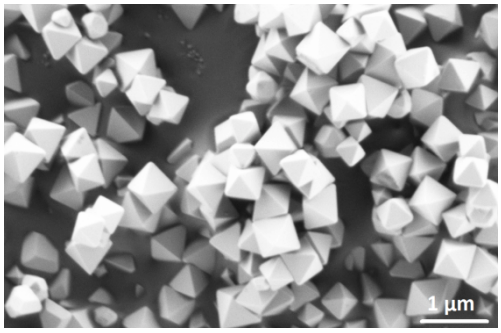

Fig. 1. FESEM image of the In_2O_3 octahedra

Moreover, these structures possess sharp edges and vertexes.

Finally, the In_2O_3 octahedra samples were subject to gas sensing tests using oxidizing (NO_2) and reducing (H_2) gases by means of DC resistance measurements performed at different operating temperatures (100-250ºC). All sensors were exposed to 15 minutes of a given concentration of a species, followed by a 30 minutes cleaning phase in dry air. All sensors showed an increase or decrease in resistance under exposure to oxidizing or reducing gases, respectively. This implies that In_2O_3 behaves as an *n*-type semiconductor.

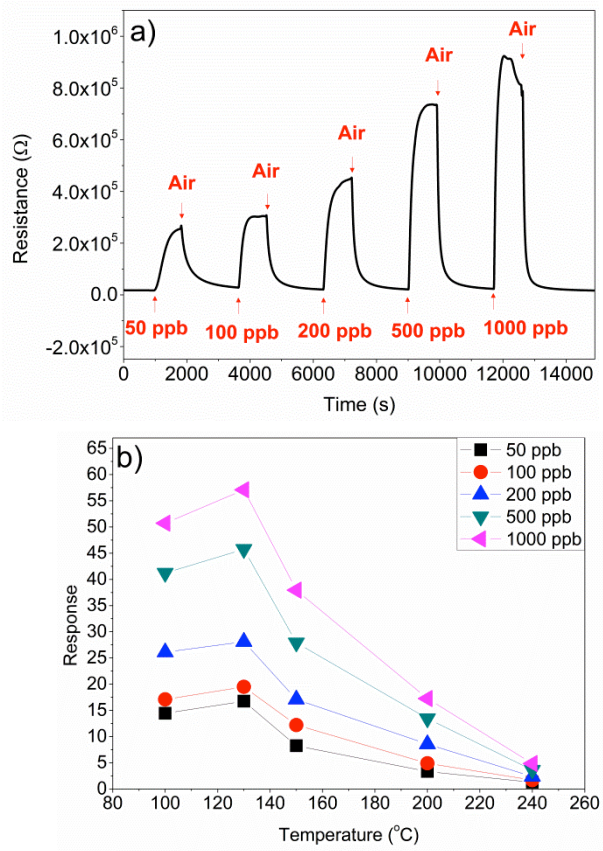

Fig. 2: (a) Response of the In_2O_3 octahedra sensor at 130ºC and (b) performance of the sensor as a function of the temperature.

As shown in Fig. 2 (b), the sensor works at optimum when operated at a relatively low temperature of 130ºC. It is important to note that our sensor is able to detect NO_2 in the range of ppb with an excellent signal to noise ratio, which means that it is possible to detect even lower concentrations of this gas (the theoretical limit of detection can be estimated at units of ppb).

Furthermore, gas sensing properties of the In_2O_3 octahedra against a reducing gas such as H_2 were investigated. The experiments were performed in the same conditions as those previously described for NO_2. Fig. 3 (a) shows the response of the sensor to low concentrations of H_2 at 200ºC. The sensor resistance decreases with increasing H_2 concentration, which is in agreement with the behavior of an *n*-type semiconductor exposed to a reducing gas. As in the case of NO_2 sensing, the signal to noise ratio is excellent for H_2 sensing, and the sensor will be able to detect concentrations in the ppb range (the theoretical limit of detection for hydrogen is in the tens of ppb range).

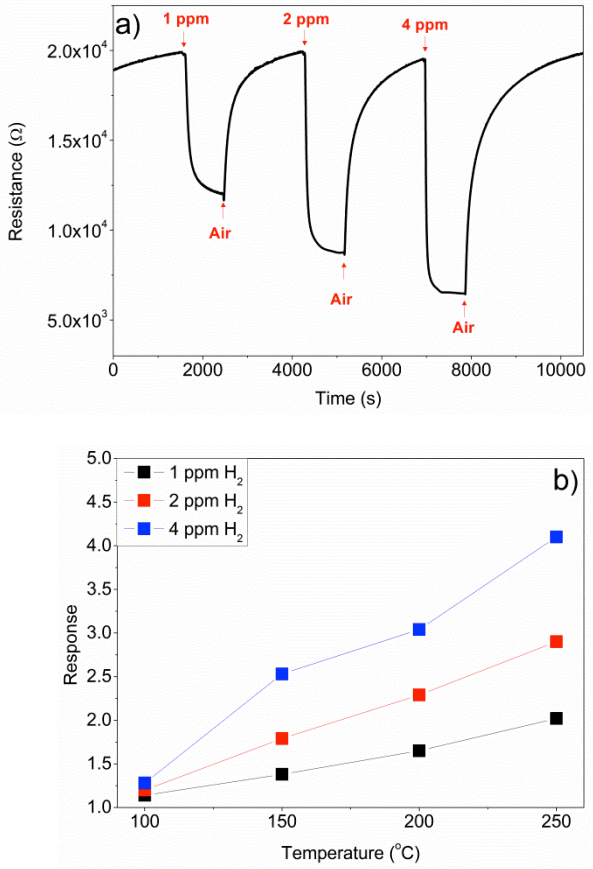

Fig. 3: (a) Response of the In_2O_3 octahedra sensor to different concentrations of H_2 at 200ºC, and (b) response of the sensor as a function of the temperature.

4. Conclusions

We have developed a facile method to synthesize high crystalline In_2O_3 octahedra at high temperatures, whose face size is around 500 nm. Additionally, we can say that pure In_2O_3 octahedra are excellent for detecting NO_2 gas with an outstanding sensitivity (0.43 ppb^{-1}) at low temperatures (130ºC), while the response to H_2 remains two orders of magnitude lower under the same conditions. In addition, the presence of humidity increases the sensitivity to NO_2 and, at the same time, reduces the response to H_2, which results in an increased selectivity. This makes our sensor an excellent candidate to detect, in a selective way, oxidizing gases such as NO_2 at low operating temperatures with an excellent sensitivity.

Synthetic challenges on the construction of QDLEDs

Sofia Paulo,[a,b] Eugenia Martinez-Ferrero,[b,*] Emilio Palomares[a,c,*]

[a]*Institute of Chemical Research of Catalonia (ICIQ), The Barcelona Institute of Science and Technology (BIST), Avinguda del Països Catalans 16, 43007 Tarragona, Spain.*
[b]*CentreFundació Eurecat. Av. d'Ernest Lluch 36, Parc Científic i de la Innovació TecnoCampus, E-08302, Mataró, Barcelona, Spain Mail: eugenia.martinez@eurecat.org.*
[c]*Catalan Institution for Research and Advanced Studies (ICREA), Passeig de Lluis Companys 23, 08010 Barcelona, Spain. Fax: +34 977920224; Tel: +34 977920200; Mail: epalomares@iciq.es.*

Abstract
During the last decades, colloidal quantum dots (QDs) have been extensively studied due to their optoelectronic properties and their potential for applications in electronic and biological systems. In our case, we have used CdSe@ZnS colloidal quantum dots as emitters in hybrid light emitted diodes (HyLEDs)[1]. Although researchers have reported high efficiencies in the last years using this architecture, there are some problems related to the fabrication on QDLEDs. One of these problems is to know how to distribute uniformly the QDs layer. In this work, we describe the problems that we have found during the fabrication of QDLED and the solutions that some researchers work with.

Introduction
As we said before, core-shell cadmium/ zinc halide quantum dots, synthetized by one-step method [2] have extraordinary optoelectronic properties, such as narrow emission and broad absorption that make of them a very interesting nanomaterial to work with. (Figure 1) Furthermore, capping with a layer of zinc sulfide (ZnS) improve their quantum efficiency and their chemical stability. Also, the easiness to tune the bandgap with the size of the quantum dot, determined by the synthetic procedure, allows the preparation of light emitting diodes from UV-vis to infrared (figure2). This color tunability increases the number of application of the QDsLED,for example as photodetector, laser applications or white light emitting diodes, combining red, green and blue QDs. (ref)

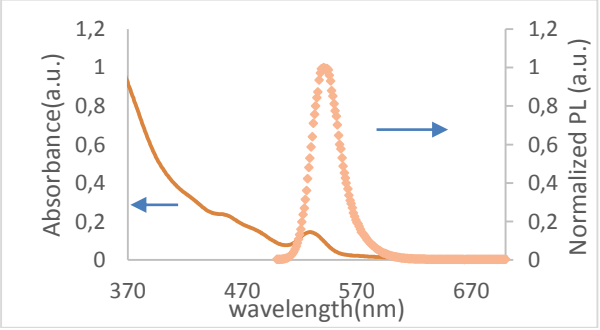

Figure 1. UV-vis spectra and emission spectra of CdSe@ZnS quantum dots in chloroform.

Thanks to their intrinsic properties as color-tunability and high-color quality saturation, they are excellent emitters in light emitting diodes. Either using normal or inverted devices structures, a vast amount of papers have been published recently on this topic with a high luminescence efficiency: For example, Ki-Hron Lee et al published a peak current efficiency of 46,4 cd/A[2] whereas Heng Zhang et al published devices with maximum luminance of 12510cd/m2.[3] Although, the good results showed, there are still some problems to make an efficient and reproducible all-solution electroluminescence device.

Discussion
In our case, we work with an inverted structure (figure 2) since this structure allows to incorporate a layer of metal oxide (ZnO) instead of poly (ethylenedioxythiophene) /polystyrenesulfonate) (PEDOT:PSS) whose acidic nature would degrade the interface with ITO rapidly. In addition we work using a bilayer or sandwich system between the emissive layer(QDs) and hole transport material., it means that the QDs layer and organic polymer layer are deposited independently. Some groups work using a solution with a mixture with QDs and the organic polymer(ref). The polymer that we work as hole transport material is poly(9-vinylcarbazole) (PVK).

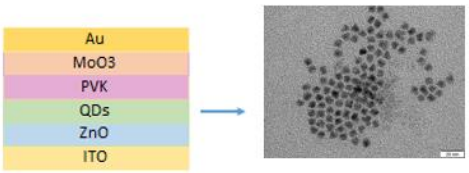

Figure 2. ***HYLED structure used in this work and TEM image of the prepared CdSe@ZnS .***

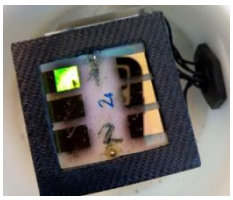

Figure 3. Green color QDLEDs prepared at Eurecat

During the fabrication steps, we found some problems related to deposited quantum dot layer. Herein, we want to describe some of them and explain some possible solution.

Compatibility between layers.[3] With the exception of MoO_3 and Au that are deposited by thermal evaporation, all the layers are deposited via spin coating conditions from solutions. For that reason, it is necessary to work with orthogonal solvents to avoid the damage between the layers. The first problem that we observe is that the majority of solvent used to dissolve the poly(9-vinylcarbazole) (PVK) degrade the layer of quantum dots, and when we deposited PVK over quantum dot layer, part of it is removed. In figure 5 appear three different photoluminescence spectra. The quantum dot emission band decreases significantly after deposition of the PVK layer that may decrease the electroluminescence efficiency.

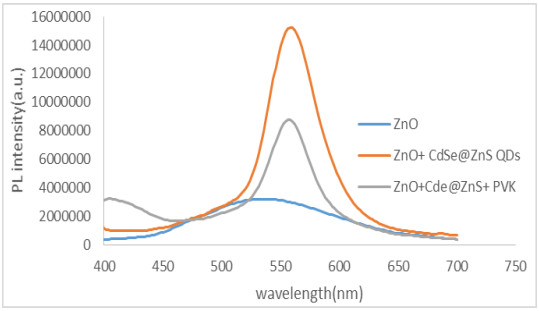

Figure 4. Photoluminescence spectra of different films.

The majority of synthesis found in the literature use oleic acid and trioctylphospine as capping ligand. So one of the possible solutions is to exchange ligands such as mercaptonoic acid (MPA) that are soluble in water.[3] The immiscibility between both solvents become a good alternative to fix that problem.

***Uniformity of the quantum dot layer*.** Other aspect that must be taken into account is the uniformity of the quantum dot layer. We observed that when we deposited a layer of quantum dots we did not obtain a homogenous layer and as consequence the recombination in the QDLED was poorer and in some cases the QDLED did not work at all. We observed that quantum dots tend to aggregate with each other forming small aggregates through the device (figure 5).

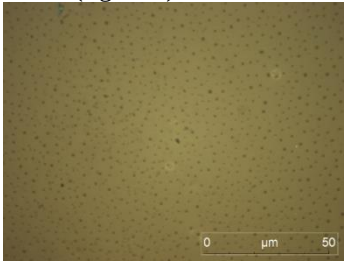

Figure 5. Picture of CdSe@ZnS. Film

One of the possible solutions that some researchers work is to incorporate a layer of PEIE or PEI between ZnO layer and quantum dots[4]. The aliphatic amine functional groups interact with the sulfurs groups of quantum dots helping to distribute uniformity de quantum dots layer. In addition, they said that PEIE / PEI help to the injection of the electrons from metal oxides to organic layers improving the efficiency of devices.[5]

***Recombination in polymer*.** Some groups have written about the double rule that quantum dots play in the device as an emitter and electron transport. So, in some cases the recombination occurs in the polymer instead of quantum dots . Some possible solutions may be to change organic polymer for other which has a higher LUMO or decrease the thickness of the hole transport material. [6]

Conclusions

Even the problems described before, the use of quantum dots in HYLEDs as a new lighting materials is a good alternative to OLEDs due to their stability, and color quality. Also, the use of cadmium free quantum dots are started to replace it in light emitted devices as emitter layer, although the efficiency still lower.

References

1. Kwak, J.; Bae, W. K.; Lee, D.; Park, I.; Lim, J.; Park, M.; Cho, H.; Woo, H.; Yoon, D. Y.; Char, K.; Lee, S.; Lee, C. Bright and Efficient Full-Color Colloidal Quantum Dot Light-Emitting Diodes Using an Inverted Device Structure. *Nano Lett.* **2012**, *12*, 2362–2366.
2. Lee, K. H.; Lee, J. H.; Kang, H. D.; Park, B.; Kwon, Y.; Ko, H.; Lee, C.; Lee, J.; Yang, H. Over 40 cd/A efficient green quantum dot electroluminescent device comprising uniquely large-sized quantum dots. *ACS Nano* **2014**.
3. Zhang, H.; Li, H.; Sun, X.; Chen, S. Inverted Quantum-Dot Light-Emitting Diodes Fabricated by All-Solution Processing. *ACS Appl. Mater. Interfaces* **2016**.
4. Son, D. I.; Kim, H. H.; Hwang, D. K.; Kwon, S.; Choi, W. K. Inverted CdSe–ZnS quantum dots light-emitting diode using low-work function organic material polyethylenimine ethoxylated.
5. Fan, C.; Lei, Y.; Liu, Z.; Wang, R.; Lei, Y.; Li, G.; Xiong, Z.; Yang, X. High-Efficiency Phosphorescent Hybrid Organic-Inorganic Light-Emitting Diodes Using a Solution-Processed Small-Molecule Emissive Layer. *ACS Appl. Mater. Interfaces* **2015**.
6. Ji, W.; Jing, P.; Zhang, L.; Li, D.; Zeng, Q.; Qu, S.; Zhao, J. The work mechanism and sub-bandgap-voltage electroluminescence in inverted quantum dot light-emitting diodes. *Sci. Rep.* **2014**, *4*, 6974.
Diodes. *ACS Nano* **2013**, *7*, 11234–11241.

Fabrication of Back-Gated Device for Gas Sensors

T.G. Welearegay, R. Calavia, R. Ionescu, E. LLobet *

MINOS-EMaS, Department of Electronics, Electrical, Automatic and Control Engineering,

Universitat Rovira i Virgili, Av. Països Catalans 26, 43007, Tarragona, Spain

Tel: +34 977 558502, Fax: +34977559605, Email: eduard.llobet@urv.cat

Abstract

In this work, we have presented a new design and configuration of gas sensor based on back-gated device that can operate at low temperature. Interdigitated gold electrodes patterned onto an oxidized, heavily doped, *p*-type silicon substrate were designed and fabricated at a wafer level. The Au –electrodes were used as source - drain metal contacts while a gate electrode was connected at the backside of the substrate. Tungsten oxide nanowires decorated with Pt nanoparticles were directly grown *via* aerosol assisted-CVD (AA-CVD) on top of the electrode area. The electrical characterization of the device in the presence of air and hydrogen gas demonstrates that the back-gated device can be used as a gas sensor operating at low temperatures.

1. Introduction

Gas sensors based on single crystalline metal oxide nanostructures (SMOx) offer many advantages in sensor performance such as high stability at typical operating temperatures, high surface to volume ratio, and tailored surface chemistry via functionalization [1, 2]. At a given high operating temperature, the surface of the sensing material gives rise to high concentration of adsorbed oxygen species which modulates the electron density at the surface and its electronic state. There has been much progress in the fabrication, and integration of different single crystalline SMOx nanostructures for gas sensing at lower temperature; as well as optimizing the minimum power consumption of such devices while maintaining high sensor performance and stability. Recently, our group has introduced highly sensitive WO_3 nanowires decorated with metal nanoparticles as sensor for reducing gases that can operate at relatively lower temperatures [3, 4].

However, some barriers to employ less power consuming resistive SMOx sensor platforms are still to be overcome. Especially, achieving SMOx devices able to work at relatively low temperature is much sought for.

Here we describe a novel configuration of a three electrode contact back-gated device for gas sensing based on Pt functionalized WO_3 nanowires for H_2 gas at low temperature.

3. Electrode Design and Fabrication

Three terminal contact electrodes, where the two interdigitated Au electrodes, sputtered and patterned onto a heavily *p*-doped, silicon substrate insulated with a thin oxide layer, were designed and fabricated at a wafer level. The interdigitated Au electrodes with 15 μm gap were then used as source-drain contacts of the FET-type sensor, while a gate electrode was configured from the backside of the substrate.

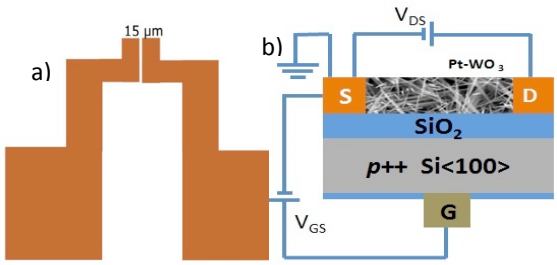

Fig.1. a) Interdigitated gold electrodes with 15 μm gap; b) back-gated sensor configuration.

A Pt heater element was printed onto alumina substrate and assembled at the backside of the Si-substrate. **Fig.1a** shows the metal contacts for source-drain electrodes (top view), and its equivalent configuration (**Fig.1b**).

4. Growth of WO_3 Nanowire

Tungsten oxide (WO_3) nanowires decorated with Pt nanoparticles were directly grown at 400 ^{0}C *via* AA-CVD from tungsten hexacarbonyl ($W(CO)_6$, 50 mg) dissolved in 15 ml of ethanol and chloroplatinic acid hydrate (H_2PtCl_6. xH_2O, 7 mg) in 5 ml of methanol. A piezoelectric ultrasonic atomizer was used to generate an aerosol of the solute and transport it to the heated substrate by N_2 gas flow at 0.5 L/min.

The as-deposited films were annealed at 450 ^{0}C in air for 2 hours, and a light white colour was observed indicating the presence of PtO on the surface of WO_3 nanowires (supported further by XPS anlysis).

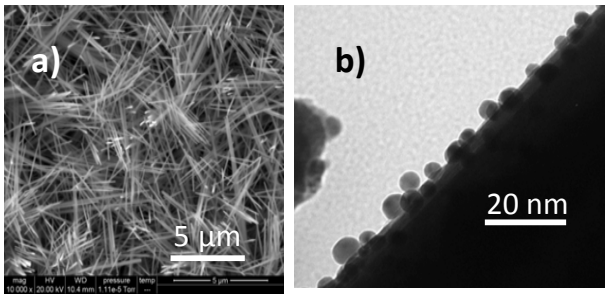

Fig.2. SEM images of the as-deposited films of; a) Pt nanoparticle decorated tungsten oxide nanoneedles (Pt-WO3x); b) the inset showing Pt nanoparticles on the surface of nanowire.

SEM images of the film showed a high density of nonaligned monoclinic WO_3 nanowires with uniform diameters near to 120 nm (**Fig.2**).

5. Results and Discussion

The back-gated device was wire bonded and mounted on a PCB support, and placed inside a test chamber for gas measurement and electrical characterization. The device was configured such that a constant voltage is applied between the source-drain, V_{DS}, while the gate potential is swept between -5 V to 5 V (sweeping rate ~ 100 mV/s). It was noted that the applied gate potential controls the electron flow along the *n*-channel developed at the oxide interface. **Fig. 3** reveals a field effect transistor (FET) behaviour of the device at a constant, V_{DS} = 1 V, and applied V_{GS} = -5 V to 5 V. The electronic surface potential of the *n*-type WO_3 nanowires were then modulated when the applied gate potential (V_{GS} < 0) depletes the majority carrier of the substrate, which minimizes electrostatic potential at the inversion layer. However, the current flow, I_{DS}, is constrained by the electric field developed at the interface of the channel, when the applied gate potential is swept to positive values (V_{GS} > 0).

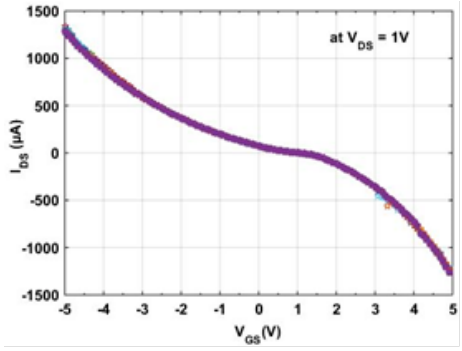

Fig.3. Characteristic I_{DS} - V_{GS} curves under dry air exposure.

Fig. 4 shows I_{DS} vs V_{GS} curve of the sensor response extracted under air and 20 ppm of H_2 gas exposures at low temperature, 100 ^{o}C.

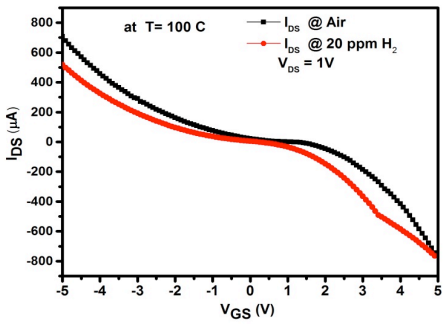

Fig.4. I_{DS} – V_{GS} curves of the sensor extracted in the presence of dry air and 20 ppm H_2 at 100 ^{0}C.

The response reveals that the surface adsorptive property of the nanowire was modulated with the applied gate potential voltage. It is worth to mention that the adsorption phenomena of H_2 gas (reducing gas) on WO_3 layer is less favoured at low temperatures generally greater than 200 ^{o}C. It is thus thought that the surface property of the nanowires could be easily tuned with an applied gate potential which could improve the sensitivity at low operating temperatures ($\Delta I_{DS}/I_{DSair}$ = 100% @ 100 ^{o}C, VGS = 3.5V).

7. Conclusions

A three contact electrode sensor device with a back-gated configuration was designed and fabricated at wafer level. Pt nanoparticle decorated WO_3 were grown onto the electrode area. The source-drain current, I_{DS}, behaviour of the device was characterized while sweeping the gate potential, which is connected onto heavily *p*-doped Si substrate. Characteristic I_{DS} vs V_{GS} plots showed that the device behaves as a field effect transistor which enables to characterize sensor response towards H_2 gas at low temperature. The results showed that this back-gated device is very promising to be employed as a *n*-channel metal oxide gas sensor operating at low temperatures.

References

[1] A. Kolakov, "Some recent trends in fabrication, functionalization, and characterization of metal oxide gas sensors". *Int. J. Nanotechnol.,* 2008, **5,** pp. 12-14.

[2] E. Comini, C. Barrato, I. Concin, G. Fagila, M. Falasconi, et al., "Metal oxide nanoscience and nanotechnology for chemical sensors". *Sens Actuators B* 2013, **179**, pp. 3-20.

[3] F.E. Annanouch, Z. Haddi, M. Ling, S. Vallejos, T. Shujah, P. Umek, C. Bittencourt, C. Blackman, E. Llobet, "Aerosol-Assisted CVD-Grown PdO Nanoparticle-Decorated Tungsten Oxide Nanoneedles Extremely Sensitive to Hydrogen". *ACS Appl. Mater. Interfaces*, 2016, **8**, pp. 10413-10421.

[4] F.E. Annanouch, Z. Haddi, S. Vallejos, P. Umek, P. Guttmann, C. Bittencourt, E. Llobet, "Aerosol-Assisted CVD-Grown WO_3 Nanoneedles Decorated with Copper Oxide Nanoparticles for the Selective and Humidity-Resilient Detection of H2S". *ACS Appl. Mater. Interfaces*, 2015, **7**, pp. 6842-6851.

Thermal noise modeling for AlGaN/GaN HEMTs

Wondwosen Eshetu Muhea*, Benjamín Iñiguez, *Senior Member, IEEE*

Dept. of Electrical Electronics and Automation Engineering, Universitat Rovira i Virgili, Spain
*Email:Wondwosen.Eshetu@urv.cat, tel.+34602059484

Abstract

In this work, RF noise model for AlGaN/GaN HEMTs based on Transmission Line method is presented. The model calculates the thermal noise, originated in the channel due to thermal random motions of charge carriers and the gate leakage current shot noise. Part of the common noise parameters are validated with experimental data.

1. Introduction

GaN based HEMTs have capability of high power handling, working in elevated temperature condition and high speed. For this reason, they are best candidates for high power, high frequency, and low noise applications including radio communications, cell phones, Voltage converters, and radar equipments [1]-[5]. Accurate RF noise model of the device is then crucial for the design of such circuits. Hence, this paper presents an RF and noise model including short channel effects.

2. RF noise model

Determining the small signal equivalent circuit components is a prerequisite for modeling noise performance of a FET device. For that purpose, a robust electrical model that is based on the device physics is needed. The starting point for the noise model presented here is the charge control compact model presented in [6].

The model is based on thorough study of the 2DEG and the interface hetro-structure and is entirely based on the physics of the device. It works for all operating regions of the device. This is useful as it gives the capability to determine the noise generated in all operating regions of the device [7].

An active line approach is adapted for the calculation of the noise. This method allows incorporating the non-quasistatic effect, the gate shot noise that arise due to gate leakage current, and the gate and drain noise correlation [8]. In previous works, it has been used for RF noise modeling of MESFETs, HEMTs, MOSFET and single gate and double gate SOI devices [8][9]. The channel is divided into small sections. Each slice of the channel is modeled by local small signal equivalent circuit together with microscopic diffusion and gate shot noise sources. An expression for each small signal component is obtained from basic semiconductor equations as given in [9].

$$C_{gc}(y) = W\Delta y\frac{\delta Q}{\delta V} \qquad g_m(y) = Wv(y)\frac{\delta Q}{\delta V}$$

$$g_c(y) = \left.\frac{\delta I_{DS}}{\delta V}\right|_{Vg=cte} \tag{1}$$

where, W is the gate width, Δy is channel section length, $Q = W\Delta yqn_s$, n_s is the 2DEG concentration, and V is potential at point x in the channel. The effect of velocity saturation is included in the above expressions.

Generalized Einstein's relationship between the differential mobility and diffusion coefficient is applied to calculate the power spectral density of the diffusion noise in each slice of the channel [9].

$$D = \frac{kT}{q}\mu_d, \quad \mu_d = \frac{dv}{dE} \tag{2}$$

where, D is the non equilibrium diffusivity, T is the noise temperature and μ_d is the differential mobility.

Based on the assumption on [9], the noise spectral current density is given as

$$S_{in}(y) = 4qWQ\frac{D}{\Delta y} = 4kTg_c(y)\,. \tag{3}$$

As the gate is a Schottky contact, there exists a current flow on the gate terminal which depends on the applied gate biasing voltage. The presence of gate leakage current in HEMTs has an effect on the small signal properties, more importantly on the noise performance of the device. It is found that traps have a vital role behind the leakage current. As a result Frankel-Poole model is used here to calculate the current density at each slice of the channel which is given as [10]

$$J_{PF} = C_{trap} E \exp(\alpha + \beta\sqrt{E}) \quad (4)$$

where, $\alpha = -\phi_d / V_{th}$ and $\beta = \sqrt{q/\pi\varepsilon_s} / V_{th}$, C_{trap} is a parameter dependent on trap concentration, ϕ_d is the barrier height, ε_s is the permittivity, and V_{th} is thermal voltage. The Electric field E is calculated using an expression given in [10].

A general analysis is implemented to solve the active transmission line and the details of the analysis are given in [9].

3. Results and Discussion

Some of the common noise parameters are compared with experimental data from [1]. The transfer characteristics of a 100nm device and the variation of the transconductance with gate voltage are shown in Fig. 1. The power spectral density of the drain thermal noise with respect to the drain current for similar device is shown in Fig. 2. An increase in drain current means an increase in the number of charge carriers. This results in an increase in the random thermal motion of charge carriers and collisions which is manifested as an increase in drain noise spectral density with respect to current as shown in Fig.2. The increasing nature of the PSD and increasing and decreasing nature of the transconductance of the device gives the minimum noise figure the shape that is shown in Fig. 3.

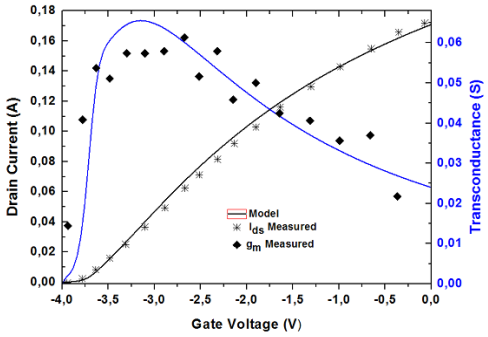

Fig. 1. DC drain current and Transconductance versus gate voltage for V_{ds}=9V. W= 2 × 100μm, L= 100nm [1].

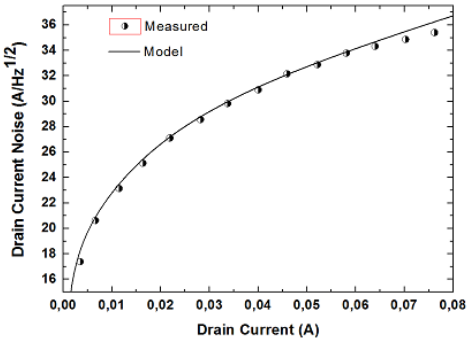

Fig. 2. Drain current noise PSD versus drain current for V_{ds}=9V, frequency = 9GHz. W= 2 × 100μm, L= 100nm [1].

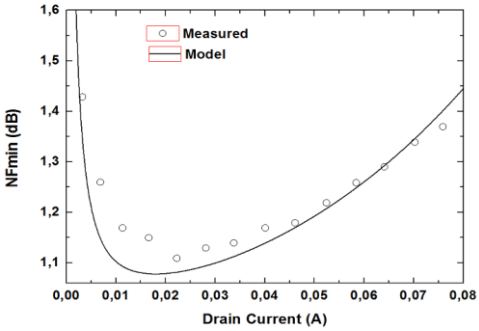

Fig. 3. Minimum noise figure versus drain current for V_{ds}=9V, frequency = 9GHz. W= 2 × 100μm, L= 100nm [1].

4. Conclusion

We have presented a physics based noise model for GaN HEMTs which is obtained using active line approach and adapting a quasi-static modeling to each slice of the channel. We discussed different noise parameters which are related with the current diffusion and gate shot noise sources that are incorporated in each section of the channel. In the future we will extend this work to include the gate noise spectral density and its correlation with drain noise.

References

[1] M. Thorsell et.al. ,"GaN-based RF power devices and amplifiers", *IEEE Trans. Microw. Theory Tech*., pp. 19-26, Jan.2009.

[2]U.Mishra et.al. ,"Thermal Study of the High-Frequency Noise in GaN HEMTs", *Proc. IEEE*, pp. 287-305, Feb.2008.

[3]Y.-F.WU et.al. ,"40-W/mm double field-plated GaN HEMTs ", in *64th Device Res. Conf.*, pp. 151-2, Jun.2006.

[4]M. Micovic et.al. ,"Robust broadband (4GHz-16GHz) GaN MMIC LNA", in *IEEE compound semiconduct. Integr. Circuits Symp*., pp. 1-4, Oct.2007.

[5]M. Rudolph et.al. ,"Analysis of the survivability of GaN low-noise amplifiers", *IEEE Trans. Microw. Theory Tech*., pp. 37-43, Jan.2007.

[6] Fetene.M.Y et.al. , "Compact charge-based physical model for current and capacitances in AlGaN/GaN HEMTs", *IEEE Tran. Electron Devices*, pp. 3746 - 3752, Nov. 2013.

[7] G. Pailloncy et.al. ,"Noise modelling in fully depleted SOI MOSFETs", *Solid-State Electron*. pp. 813-25, May 2004.

[8] A.Lazaro, B. Iñiguez, "RF and noise model of gate-all-around MOSFETs", *Semicond.Sci.Technol*., pp. 12, May. 2008.

[9] A.Lazaro, B. Iñiguez, "RF and noise performance of double gate and single gate SOI", *Solid-State Electron*, pp. 826-42, Mar. 2006.

[10] S.Ghosh et.al. ,"Surface-Potential-Based compact modelling of gate current in AlGaN/GaN HEMTs", *IEEE Tran. Electron Devices*, pp. 443-48, Feb. 2015.

From raw data to biological insights: data processing in mass spectrometry-based metabolomics.

Xavier Domingo-Almenara[1], Alexandre Perera[2], Jesus Brezmes[1]

[1]Metabolomics Platform - CIBER-DEM, Dept. of Electric Engineering (DEEEA), Universitat Rovira i Virgili, Tarragona, Catalonia, Spain

[2]B2SLAB, CIBER-BBN, ESAII, Universitat Politècnica de Catalunya, Barcelona, Catalonia, Spain

Metabolomics is now widely used to obtain new insights into human, plant and microbial biochemistry, as well as in drug discovery, nutrition research and food control through the study of the organism's metabolome. Nowadays, different analytical techniques including nuclear magnetic resonance spectroscopy (NMR) or other hyphenated techniques such as gas or liquid chromatography coupled to mass spectrometry (GC-MS and LC-MS), are used for compound profiling in metabolomics. In fact, different analytical techniques are needed as no analytical platform covers the full metabolome.

One of the major bottlenecks in metabolomics is to convert raw data samples into biological interpretable information. Also, mass spectrometry-based metabolomics generates large and complex datasets characterized by co-eluting compounds and with experimental artifacts. In order to identify and extract quantitative information of metabolites across multiple biological samples, workflows for GC–MS data processing are needed. GC–MS data processing steps include a pre-processing, comprised of noise filtering and baseline removal of chromatograms, peak-picking or deconvolution of compounds and their alignment across samples, and the identification of metabolites by spectral library matching.

Independent component analysis – orthogonal signal deconvolution (ICA–OSD) was recently introduced [1,2] to improve the capabilities of the current strategies that tackle the deconvolution step in the metabolomics workflow. The typical approach of the ICA-based methods for GC–MS data processing is based on considering the spectra as the independent component in the chromatogram. In ICA–OSD, the concept of independence was twisted: compound profiles were targeted as the independent source of the chromatographic mixture, as opposite to the spectra.

However, multivariate methods performance such as multivariate curve resolution or ICA depend, to a greater degree, on an appropriate estimation of the number of components to build the multivariate model. This bottleneck has limited the use of multivariate methods in high-throughput GC-MS data processing tools. Recently, a multivariate compound detector to detect compounds instead of peaks was introduced, which, in conjunction with OSD, lead to an innovative spectral deconvolution of compounds in GC–MS mixtures without the use of factor analysis techniques.

Finally, despite the existence of different pieces of free and commercial software for GC–MS data analysis, none of these allow the execution of an integrated workflow that includes spectral deconvolution and alignment, followed by the identification and quantification of metabolites in the same application, and implemented in a modularized and standardized manner. These new methodologies for spectral deconvolution were embedded in the eRah R package [3], which was demonstrated to be capable of conducting the complete metabolomics workflow for GC–MS, including pre-processing, spectral deconvolution, alignment and identification. eRah was able to convert raw data into biological interpretable information and thus, allowed resolving biological answers and discovering new biological insights.

References

[1] Domingo-Almenara X, Perera A, Ramírez N, Cañellas N, Correig X, Brezmes J. "Compound identification in gas chromatography/mass spectrometry-based metabolomics by blind source separation". *Journal of Chromatography A* **(2015).** Vol. 1409: 226-233.

[2] Domingo-Almenara X, Perera A, Ramírez N, Brezmes J. "Automated resolution of chromatographic signals by independent component analysis - orthogonal signal deconvolution in comprehensive gas chromatography/mass spectrometry-based metabolomics". *Computer Methods and Programs in Biomedicine* **(2016).** Vol. 130, 135-141.

[3] Domingo-Almenara X, Brezmes J, Vinaixa M, Samino S, Diaz M, Ibanez L, Correig X, Perera A, Yanes O. "eRah: a computational tool integrating spectral deconvolution and alignment with quantification and identification of metabolites in GC-MS-based metabolomics." (Submitted).